Draft version May 3, 2022
Typeset using LaTeX default style in AASTeX631

arXiv:2205.00113v1 [astro-ph.GA] 30 Apr 2022

An ALMA study of the massive molecular clump N159W-North in the Large Magellanic Cloud: A possible gas flow penetrating one of the most massive protocluster systems in the Local Group

Kazuki Tokuda,[1,2,3] Taisei Minami,[3] Yasuo Fukui,[4] Tsuyoshi Inoue,[5] Takeru Nishioka,[4] Kisetsu Tsuge,[6] Sarolta Zahorecz,[2] Hidetoshi Sano,[7,2] Ayu Konishi,[3] C.-H. Rosie Chen,[8] Marta Sewiło,[9,10,11] Suzanne C. Madden,[12] Omnarayani Nayak,[13] Kazuya Saigo,[14] Atsushi Nishimura,[15] Kei E. I. Tanaka,[16,2] Tsuyoshi Sawada,[2,17] Remy Indebetouw,[18,19] Kengo Tachihara,[4] Akiko Kawamura,[2] and Toshikazu Onishi[3]

[1] *Department of Earth and Planetary Sciences, Faculty of Sciences, Kyushu University, Nishi-ku, Fukuoka 819-0395, Japan*
[2] *National Astronomical Observatory of Japan, National Institutes of Natural Sciences, 2-21-1 Osawa, Mitaka, Tokyo 181-8588, Japan*
[3] *Department of Physics, Graduate School of Science, Osaka Metropolitan University, 1-1 Gakuen-cho, Naka-ku, Sakai, Osaka 599-8531, Japan*
[4] *Department of Physics, Nagoya University, Furo-cho, Chikusa-ku, Nagoya 464-8601, Japan*
[5] *Department of Physics, Konan University, Okamoto 8-9-1, Kobe, Japan*
[6] *Dr. Karl Remeis Observatory and ECAP, Universität Erlangen-Nürnberg, Sternwartstrasse 7, 96049, Bamberg, Germany*
[7] *Faculty of Engineering, Gifu University, 1-1 Yanagido, Gifu 501-1193, Japan*
[8] *Max Planck Institute for Radio Astronomy, Auf dem Huegel 69, D-53121 Bonn, Germany*
[9] *CRESST II and Exoplanets and Stellar Astrophysics Laboratory, NASA Goddard Space Flight Center, Greenbelt, MD 20771, USA*
[10] *Department of Astronomy, University of Maryland, College Park, MD 20742, USA*
[11] *Center for Research and Exploration in Space Science and Technology, NASA Goddard Space Flight Center, Greenbelt, MD 20771, USA*
[12] *AIM, CEA, CNRS, Université Paris-Saclay, Université Paris Diderot, Sorbonne Paris Cité, F-91191 Gif-sur-Yvette, France*
[13] *Space Telescope Science Institute, Baltimore, MD 21218, USA*
[14] *Department of Physics and Astronomy, Graduate School of Science and Engineering, Kagoshima University, 1-21-35 Korimoto, Kagoshima, Kagoshima 890-0065, Japan*
[15] *Nobeyama Radio Observatory, National Astronomical Observatory of Japan (NAOJ), National Institutes of Natural Sciences (NINS), 462-2 Nobeyama, Minamimaki, Minamisaku, Nagano 384-1305, Japan*
[16] *Center for Astrophysics and Space Astronomy, University of Colorado Boulder, Boulder, CO 80309, USA*
[17] *Joint ALMA Observatory, Alonso de Córdova 3107, Vitacura, Santiago 763-0355, Chile*
[18] *Department of Astronomy, University of Virginia, PO Box 400325, Charlottesville, VA 22904, USA*
[19] *National Radio Astronomy Observatory, 520 Edgemont Rd, Charlottesville, VA 22903, USA*

ABSTRACT

Massive dense clumps in the Large Magellanic Cloud can be an important laboratory to explore the formation of populous clusters. We report multiscale ALMA observations of the N159W-North clump, which is the most CO-intense region in the galaxy. High-resolution CO isotope and 1.3 mm continuum observations with an angular resolution of $\sim 0\farcs25$ ($\sim$0.07 pc) revealed more than five protostellar sources with CO outflows within the main ridge clump. One of the thermal continuum sources, MMS-2, shows especially massive/dense nature whose total H_2 mass and peak column density are $\sim 10^4\,M_\odot$ and $\sim 10^{24}\,\mathrm{cm}^{-2}$, respectively, and harbors massive ($\sim 100\,M_\odot$) starless core candidates identified as its internal substructures. The main ridge containing this source can be categorized as one of the most massive protocluster systems in the Local Group. The CO high-resolution observations found several distinct filamentary clouds extending southward from the star-forming spots. The CO (1-0) data set with a larger field of view reveals a conical-shaped, $\sim$30 pc long complex extending toward the northern direction. These features indicate that a large-scale gas compression event may have produced the massive star-forming complex. Based on the striking similarity between the N159W-North complex and the previously reported other two high-mass star-forming clouds in the nearby regions, we propose a "teardrops inflow model" that explains the synchronized, extreme star formation across >50 pc, including one of the most massive protocluster clumps in the Local Group.

Keywords: ISM: clouds ISM: kinematics and dynamics ISM: molecules stars: formation

1. INTRODUCTION

High-mass stars and the associated events in their formation and evolution dramatically change the surrounding interstellar environment and eventually regulate galaxy evolution. Its astrophysical importance has motivated a large number of both observational and theoretical efforts in the past few decades (see reviews by e.g., Zinnecker & Yorke 2007; Tan et al. 2014). One of the basic ideas to explain the formation of an individual high-mass star or binary/multiple systems is that a massive cloud core, whose mass is $\sim$100 $M_\odot$, collapses into stellar objects in a similar manner to low-mass star formation (e.g., McKee & Tan 2003). The dynamical process produces more massive protostellar disks and more energetic outflow than those in the low-mass case (e.g., Matsushita et al. 2017), which is consistent with recent observational findings achieved by millimeter/submillimeter facilities (e.g., Beuther et al. 2002; Hirota et al. 2017; Matsushita et al. 2019; Motogi et al. 2019; Tanaka et al. 2020; Torii et al. 2021).

Because most stars form as clusters (e.g., Lada & Lada 2003), understanding the cluster formation mechanism is a key toward establishing the conclusive picture of high-mass star formation. The 24 most massive giant molecular clouds (GMCs) are currently responsible for most of the star formation in the Galaxy (Lee et al. 2012), assuming the GMCs will make clusters. Observational characterizations of such massive cradles forming young massive clusters (YMC) whose total stellar mass exceeds $\sim 10^4\,M_\odot$ (Portegies Zwart et al. 2010) are thus a reasonable approach to investigate their formation origin. According to the review by Longmore et al. (2014), "in-situ star formation" requires sufficient gas to be packed into the final cluster volume, and thus predicts the formation of a starless massive clump before the onset of extreme star formation. The mass and size (radius) requirements are $\gtrsim 10^4\,M_\odot$ and $\lesssim$1 pc, respectively. Although the probability of discovering a completely starless phase is very small due to the extremely short lifetime (Motte et al. 2018; Vázquez-Semadeni et al. 2019, and references therein), there should be a sufficient number of ongoing star-forming clouds (Ginsburg et al. 2012). In order to form such massive clouds, mass accumulation, i.e., gas flow, from a large-scale surrounding environment is necessary, and some promising mechanisms have been proposed, mainly motivated by observations, such as cloud-cloud collision (Fukui et al. 2021), and global hierarchical collapse (Motte et al. 2018). Revealing a high-dynamic-range molecular gas spatial/velocity distribution from a giant molecular cloud to an individual core inside the parental cloud is still a key method to further consider what mass accumulation mechanism is efficiently working at each physical scale.

The most nearby cluster-forming regions, such as Orion, whose distance from the Sun is $\lesssim$1 kpc, are not necessarily appropriate to pursue the YMC formation judging from the current gas distribution and star formation activities therein (Portegies Zwart et al. 2010). In this regard, several outstanding regions along with the Galactic disk, e.g., Cygnus X, Carina, W43, W49, and W51, are the nearest neighbors as extreme star-forming environments, because they have a sufficient molecular gas mass, $\gtrsim 10^6\,M_\odot$ (e.g., Nguyen-Luong et al. 2016). Unfortunately, almost all of these regions are located within a $\pm 1^\circ$ galactic latitude range on the inner Galactic plane where line-of-sight contaminations from unrelated objects are significant. Because dense clumps/cores rarely appear by chance in the same observed direction, source confusion may not have serious impact on such a small-scale study itself. However confusion from larger ($\gtrsim$10 pc) scale foreground/background emission to individual massive clumps makes it difficult to examine the formation mechanisms of progenitors leading to YMCs in these outstanding Galactic regions. Extragalactic targets at a distance of $\lesssim$100 kpc can be a frontier to obtain a much clearer view around YMC progenitor clumps. Atacama Large Millimeter/submillimeter Array (ALMA) provides an unprecedented view resolving individual proto/prestellar sources with a spatial resolution of $\lesssim$0.1 pc (e.g., Indebetouw et al. 2020).

The Large Magellanic Cloud (LMC) is one of the ideal laboratories to investigate molecular clouds clearly thanks to its proximity (D $\sim$50 kpc, Schaefer 2008; de Grijs et al. 2014) and face-on view (Balbinot et al. 2015). The star formation activity is different from that in the Galaxy; populous clusters are actively forming (e.g., Hodge 1961; van den Bergh 1981). Their stellar masses are 10^4–$10^5\,M_\odot$, which is larger than those of Galactic open clusters (Kumai et al. 1993; Hunter et al. 2003). The most extreme star-forming region is 30 Dor, which is the brightest H II region in the galaxy, inhering a total stellar mass of $\sim 10^5\,M_\odot$ (e.g., Cignoni et al. 2015). However, the total amount of the remaining molecular material in this region is $\sim 10^5\,M_\odot$ (e.g., Minamidani et al. 2008, 2011; Wong et al. 2011), which is not large compared to the above-listed GMCs in the Galaxy. Among the $\sim$300 entities discovered by the NANTEN CO(1–0) survey in the LMC (Fukui et al. 2008; Kawamura et al. 2009), the molecular cloud associated with the N159 H II region (hereafter, the N159 GMC) is the most massive one with a total gas mass of $\sim 2 \times 10^6\,M_\odot$ and a less evolved region than 30 Dor (see also Johansson et al. 1994, 1998).

Using the single-dish Atacama Submillimeter Telescope Experiment (ASTE), Minamidani et al. (2008) performed CO(3–2) observations on several GMCs along the molecular ridge region at the south-east side of the galaxy and

confirmed that the N159W cloud shows the strongest intensity. The subsequent comprehensive CO(1–0) study with the Mopra telescope (Wong et al. 2011) also confirmed that it shows the strongest peak along with the N113 region. Using the same telescope, Nishimura et al. (2016) reported marginal detections of N_2H^+ emission in N159W and N113 despite of a significant deficient of N-bearing molecules in LMC (Millar & Herbst 1990). Measurements at millimeter/submillimeter windows (Paron et al. 2016; Galametz et al. 2020) detected several high-density gas tracers, HCO^+, HCN, CS, and (tentative) $C^{18}O$, toward the N159W region. Ott et al. (2010) performed an NH_3 survey on such CO prominent regions, including N159W and N113, using the Australia Telescope Compact Array (ATCA). The NH_3 emission was only found in the N159W-North region, indicating the molecule is also deficient in the LMC, and likely traces the densest best-shielded cores. The CO peak and the position of NH_3 core is $\sim$10 pc displaced from the Hα peak (e.g., Smith & MCELS Team 1999), indicating that the molecular gas dissipation has not been started yet. Nevertheless, the Spitzer-based studies discovered several luminous ($\gtrsim 10^5\,L_\odot$) young stellar object (YSO) candidates inside the cloud (e.g., Seale et al. 2009, 2014; Gruendl & Chu 2009; Chen et al. 2010; Carlson et al. 2012; Jones et al. 2017). These observational signatures strongly demonstrate that active star formation is ongoing in the massive cloud and its evolutionary stage must be early.

Early ALMA observations in Cycle 1 clearly revealed molecular filaments in the N159W and N159E regions (Fukui et al. 2015; Saigo et al. 2017). Figure 1 shows an overview of the ALMA CO observations in N159E/W. One of the interesting findings is that the locations of the bright YSOs are the intersections of multiple filamentary clouds, which partially resemble galactic hub filaments (e.g., Myers 2009; Peretto et al. 2013). The N159 studies hypothesized that filament-filament collisions promoted high-mass star formation activity (Fukui et al. 2015; Saigo et al. 2017). The follow-up ALMA high-resolution studies in Cycle 4 toward N159E-Papillion (Fukui et al. 2019, hereafter Paper I; Sharda et al. 2021) and N159W-South (Tokuda et al. 2019, hereafter Paper II) further resolved complex web-type systems with a filament widths of $\sim$0.1 pc (Figure 1b,c). Papers I and II concluded that the coalescence/collision of many individual filaments is unlikely to form such a complex system almost simultaneously across 50 pc. Alternatively, they suggested that a large-scale H I gas flow driven by the last tidal interaction between the LMC and Small Magellanic Cloud (SMC) triggered the filament and subsequent high-mass star formation at the two systems in N159E/W.

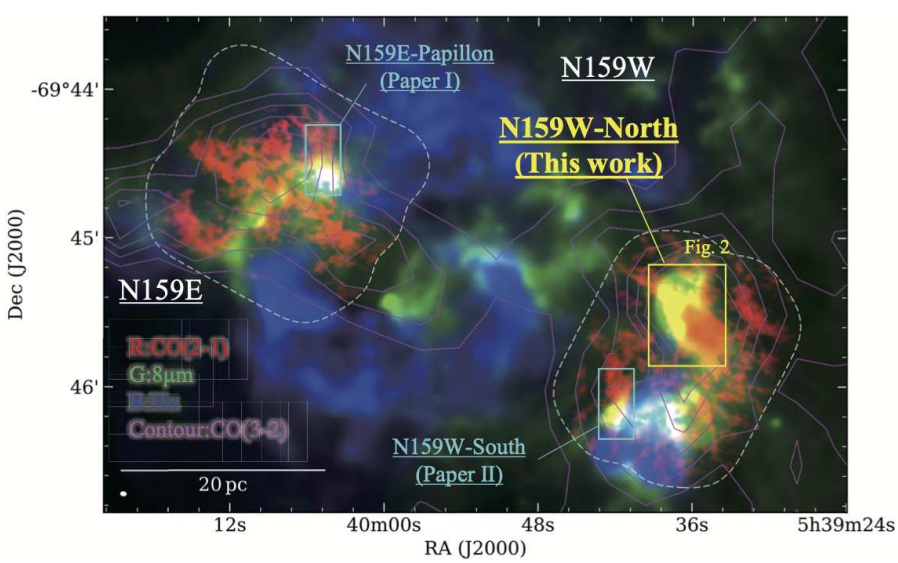

Figure 1. A multi-wavelength overview of N159E/W. (a) Three-color composite image combining the ALMA Cycle 1 ^{12}CO (J = 2–1) (red; Fukui et al. 2015; Saigo et al. 2017; Nayak et al. 2018), the Spitzer/IRAC 8.0 μm (green; Meixner et al. 2006), and the MCELS Hα (blue; Smith & MCELS Team 1999) images. Regions delimited by white dashed lines represent the ALMA Cycle 1 field coverages. The white ellipse in the lower left corner gives the ALMA beam size of $1\farcs3 \times 0\farcs8$. The magenta contours show the ^{12}CO(J = 3–2) integrated intensity map with ASTE (Minamidani et al. 2008). The lowest and subsequent contour steps are 10 K km s^{-1}.

The present study is the third paper to show the same observing project with Papers I and II, but we describe the high-resolution ($\sim 0\farcs26$) ALMA 1.3 mm wavelength CO, its isotopes, and continuum images in the N159W-North

region for the first time. The total molecular gas mass of star-forming dense clump are one order of magnitude larger than the previously reported two regions (see the comparison in Sect. 3.3). Taking into account the fact that high-density gas tracers such as NH_3 have also been detected, this region is even more favorable for exploring the formation of massive dense clump leading to YMC. We also present one more additional data set, CO(1–0), at a lower resolution ($\sim$1.″5) covering a wide field coverage. Section 2 explains the observations and data reduction. Section 3 provides a multiscale molecular cloud view from $\sim$100 pc down to $\sim$0.06 pc and characterizes the individual proto/prestellar cores. Section 4 discusses the formation scenario of the massive clump in the N159W-North region as well as the high-mass star formation throughout the N159 E/W region.

2. OBSERVATIONS AND DATA REDUCTION

In the ALMA Cycle 4, we carried out Band 6 (211–275 GHz) observations toward the N159W-North region with the ALMA 12 m array as part of a multiobjects survey in N159 (P.I.: Y. Fukui #2016.1.01173.S). Because the previous studies (Papers I and II) described the observation and data reduction details, we briefly summarize the data quality here. The frequency setting mainly targeted the molecular lines of ^{12}CO(J = 2–1), ^{13}CO(J = 2–1), C^{18}O(J = 2–1) and 1.3 mm continuum. The synthesized beam sizes of the ^{12}CO line and continuum images are 0.″27 × 0.″23, and 0.″26 ×0.″23, respectively. The rms noise (1σ) levels of the ^{12}CO line and the continuum are $\sim$3.7 mJy beam^{-1} ($\sim$1.3 K) at a velocity resolution of 0.2 km s^{-1} and $\sim$0.027 mJy beam^{-1}. Table 5 in Appendix A presents the beam propeties and sensitivities of the analyzed lines in this paper. Because the ^{12}CO and ^{13}CO emission of the N159W-North region in the Cycle 4 data have non negligible missing flux ($\sim$40–60%), we used the combined data with the new Cycle 4 and the previously obtained Cycle 1 data sets (Fukui et al. 2015; Nayak et al. 2018) throughout the manuscript. Note that the previously obtained CO sets did not include the compact array (7 m+TP) data, but the 12 m array data alone sufficiently covers the total flux judging from single-dish measurements in this region (see Fukui et al. 2015; Nayak et al. 2018).

In addition to the Band 6 data, we retrieved an ALMA archival Band 3 (84–116 GHz) CO(J = 1–0) data (P.I.: T. Sawada #2019.1.00915.S) of the same source covering a much larger spatial scale. The field coverage was 170″ × 180″ centered at ($\alpha_{\rm J2000.0}$, $\delta_{\rm J2000.0}$) = (5$^{\rm h}$39$^{\rm m}$35.$^{\rm s}$0, −69°45.″31.″2). Using CASA (Common Astronomy Software Application) version 5.6.1, we individually imaged the 12 m, 7 m , and TP(Total Power) array data and then combined them together using the `feather` task. The resultant beam size and sensitivity of the CO(J = 1–0) data cube are 2.″2 × 1.″8 and $\sim$0.6 mJy beam^{-1} ($\sim$1.5 K) at a velocity resolution of 0.2 km s^{-1}. Note that we made all of the molecular line cube data in a unified velocity frame of LSRK (Local Standard of Rest, Kinematic), and describe the velocity in the same frame throughout the manuscript.

3. RESULTS

3.1. *High-resolution ^{12}CO and ^{13}CO images of the N159W-North region*

Figure 2 shows peak brightness temperature maps of ^{12}CO and ^{13}CO(J = 2–1) at a spatial resolution of $\sim$0.06 pc. The high-spatial dynamic range observations have revealed the molecular cloud distribution with a size scale of $\sim$10 pc down to $\lesssim$0.1 pc (the velocity-channel maps are presented in Figures 10 and 11 of Appendix B). Within the molecular cloud, there are at least two spectroscopically confirmed YSOs, whose luminosity are $\sim$10^5 $L_\odot$ identified by the infrared observations using Spitzer (e.g., Seale et al. 2009; Gruendl & Chu 2009; Chen et al. 2010; Seale et al. 2014; Jones et al. 2017). In this paper, we call the two sources as YSO-N1 and YSO-N2, which are 053937.56-694525.4 and 053937.04-694536.7, respectively, in the Chen et al. (2010) catalog. For the two YSOs, we detected 1.3 mm continuum emission (see black contours in Figure 2), tracing free-free emission from ionized gas and/or thermal dust components in the cold/dense condensations (see more details in Sect. 3.2). With respect to the continuum and YSO sources, the ^{12}CO and ^{13}CO cloud asymmetrically distributes in the northwest(NW)-southeast(SE) direction. We see a highly extended emission on the NW side, while the SE region has a sharp boundary at the cloud edge.

The ^{12}CO peak brightness temperature map (Figure 2a) shows that most of the emitting area exceed 30 K and the maximum value is $\sim$80 K. Assuming the abundance (isotope) ratio, ^{12}CO/^{13}CO of 50 (Johansson et al. 1994; Mizuno et al. 2010), the typical intensity ratio between ^{12}CO and ^{13}CO of $\sim$2 tells us that the optical thickness of ^{12}CO is $\gtrsim$30, which is an optically thick regime. The peak brightness map in ^{12}CO thus reflects the temperature distribution in this region under the local thermodynamical equilibrium (LTE) assumption. The most intense region is around YSO-N2, but the area near the cloud edge at the SE side is also uniformly high, $\sim$50 K. In addition to the feedback from YSO-N1, there may be some heating mechanisms changing the temperature of the molecular cloud

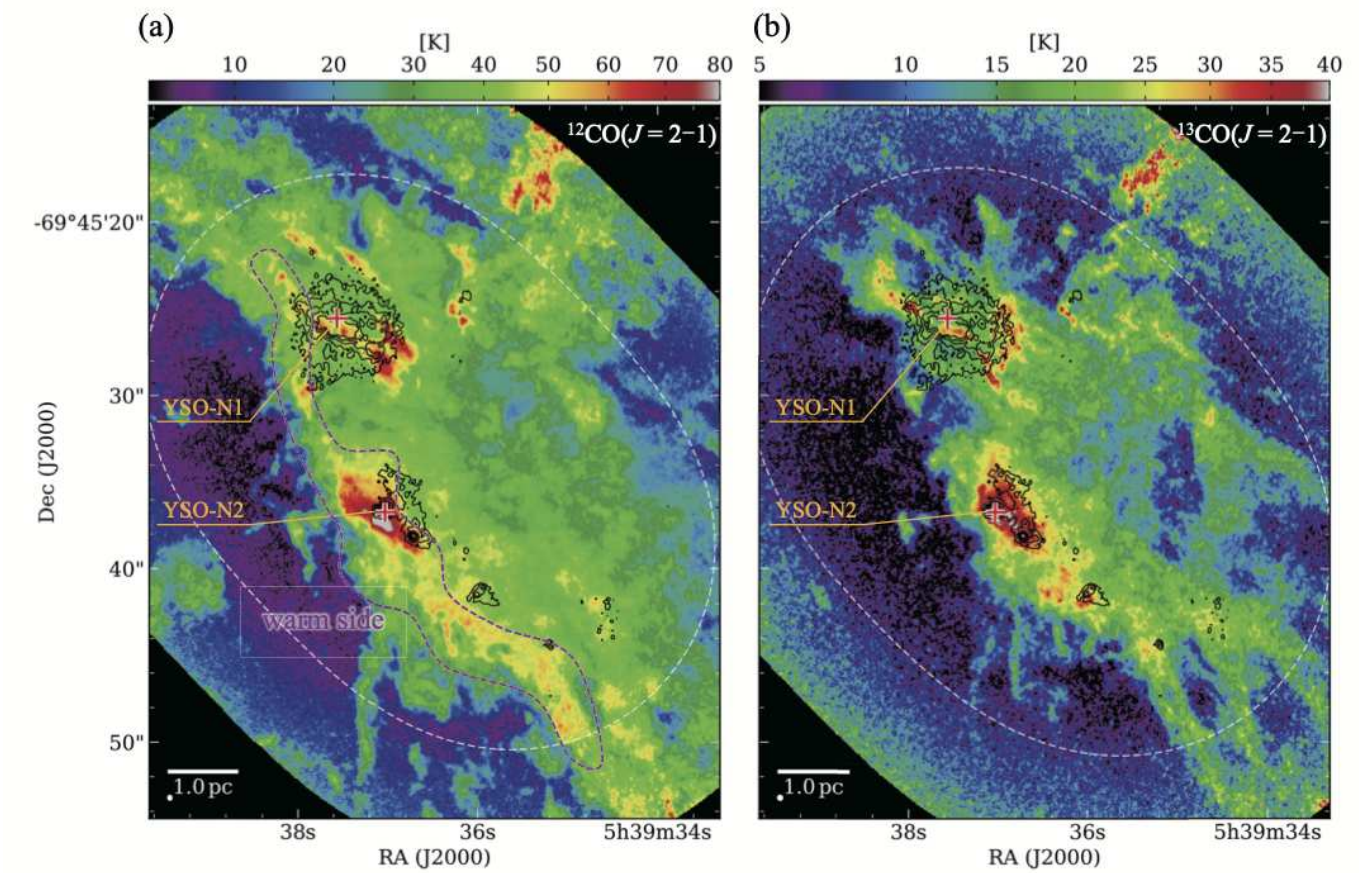

Figure 2. (a) The color-scale image illustrates the ^{12}CO(J = 2–1) peak brightness temperature map. The white ellipse in the lower-left corner gives the angular resolution, $0\farcs27 \times 0\farcs23$. The white dashed ellipse indicates where the mosaic sensitivity falls to 50%. The purple dashed line marks the warm side of the cloud (see details in Sect. 4.1.2). The black contours show the 1.3 mm continuum image. The lowest contour and subsequent steps are 0.1 mJy beam^{-1}. The red crosses denote positions of two YSOs (Chen et al. 2010). (b) Same as (a) but for the ^{13}CO(J = 2–1) peak brightness temperature map.

across several parsecs. We call the distinct feature "warm side" hereafter as indicated in the dotted line in Figure 2a and discuss the possible origins in Sect. 4.1.2.

^{13}CO emission is optically thin at a molecular cloud scale generally, and thus it is a good tracer of column density. The LTE calculation (Rohlfs & Wilson 2004) tells us that the median and maximum H_2 column densities are $\sim$3 $\times 10^{23}$ cm^{-2} and $\sim$1 $\times 10^{24}$ cm^{-2}, respectively, assuming $[H_2]/[^{13}CO] = 3\times10^6$ for consistency with the previous analysis (e.g., Mizuno et al. 2010). Adopting the mean molecular weight per hydrogen molecule (2.8), the total H_2 gas mass is $\sim 7\times 10^4\, M_\odot$ within the ^{13}CO detected region above 5σ noise level on the integrated intensity image. This mass is almost comparable to a single giant molecular cloud traced by ^{13}CO(J = 2–1) (e.g., the Orion A cloud; Nishimura et al. 2015).

3.1.1. *Filaments extending from the main ridge*

One of the notable characteristics in the ^{12}CO and ^{13}CO images (Figure 3) is that there are several filamentary structures, which extend to the south direction from the vicinity of YSO-N1 and N2. We call these features as "filaments", hereafter. Only filament D has a discontinuous distribution with weaker intensity than the others and is not detected in ^{13}CO, and thus we treat it as marginal. The projected lengths of the ^{12}CO and ^{13}CO filaments are $\sim$4 pc and $\sim$3 pc, respectively. Since we could not measure the actual length of the ^{12}CO filaments, especially for A and B, due to the limited field coverage (Figure 3), the current estimate is thus the lower limit. The column density and line masses of the filaments are $\sim(2\text{–}6)\times10^{22}$ cm^{-2} and $\sim(1\text{–}3)\times10^2\, M_\odot$ pc^{-1}, respectively, which are listed in Table 1.

The velocity-widths, Δv are $\sim$1–3 km s^{-1} in FWHM, corresponding to velocity-dispersion, σ_v ($= \Delta v/2\sqrt{2\ln 2}$) of 0.4–1.3 km s^{-1}. The virial line masses of the filaments, $M_{\rm line,vir} = 2\sigma_v^2/G$, are calculated to be (0.9–8) $\times 10^2\, M_\odot$ pc^{-1}, which is somewhat larger than those values obtained from the ^{12}CO luminosity mass mentioned above. Sect. 4.1.1 discuss the formation of these filaments and the relation between them and the star formation in this region.

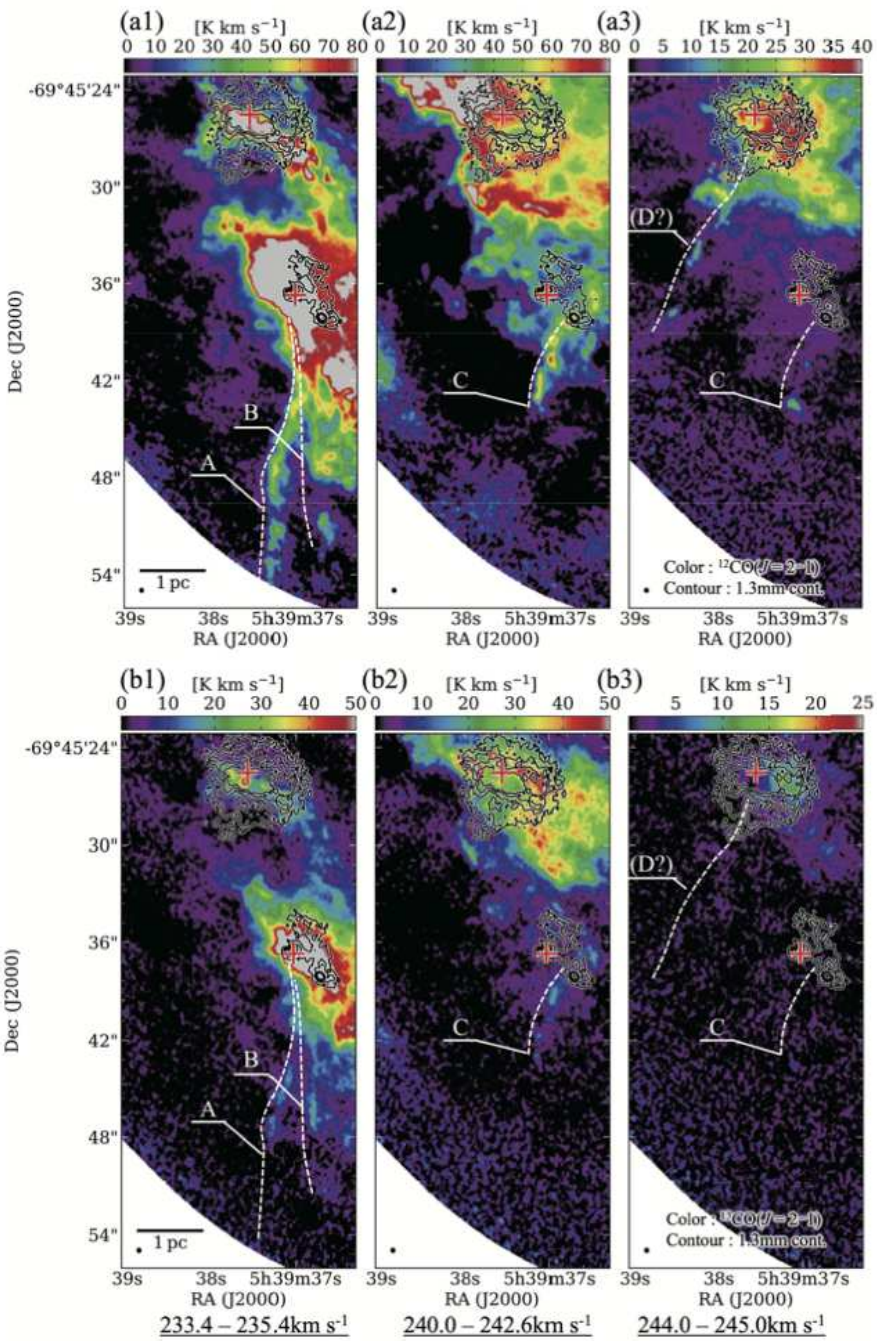

Figure 3. Spatial distributions of the filaments in the N159W-North region. (a1–a3) The color-scale images illustrate the velocity channel maps of the ^{12}CO(J = 2–1) with velocity ranges of 232.0–234.0 km s^{-1} (a1), 240.0–242.6 km s^{-1} (a2), and 244.0–245.0 km s^{-1} (a3). The ellipse at the lower-left corner in each panel gives angular resolution, 0.″27 × 0.″23. White dashed lines highlight the filaments by eye. Red crosses denote the positions of YSO, same as those in Figure 2. (b1–b3) Same as panels (a1–a3), but for the ^{13}CO(J = 2–1) maps.

Table 1. Physical quantities of filaments traced in ^{12}CO(J = 2–1)

filament name	$v_{\rm cent}$ [km s^{-1}]$^{\rm a}$	Δv [km s^{-1}]$^{\rm a}$	L [pc]$^{\rm b}$	M [$M_\odot$]$^{\rm c}$	$N_{\rm H_2}^{\rm ave}$ [cm^{-2}]$^{\rm c}$	$M_{\rm line}$ [$M_\odot$ pc^{-1}]$^{\rm d}$
A	232.3	2.3	3.5	4×10^2	2×10^{22}	1×10^2
B	234.5	2.4	2.9	4×10^2	2×10^{22}	1×10^2
C	242.4	3.1	1.9	3×10^2	2×10^{22}	1×10^2
D	244.0	1.1	...$^{\rm e}$	2×10^2	2×10^{22}	...$^{\rm e}$

[a] Central velocity ($v_{\rm cent}$) and width in FWHM (Δv) determined by a single Gaussian fitting to the ^{12}CO spectra at the cyan cross positions in panels (a,b) of Figure 3.

[b] Projected length between the southern edge of filaments and the boundary of the main ridge (see also the definition of the main ridge in Sect. 3.3).

[c] ^{12}CO luminosity based total mass and averaged column density of each filament. We assumed a constant conversion factor of $X_{\rm CO} = 5\ \times10^{20}\,{\rm cm^{-2}\,(K\,km\,s^{-1})^{-1}}$ (Hughes et al. 2010) and CO(2–1)/CO(1–0) intensity ratio of 1.0.

[d] Line mass inferred from M/L.

[e] We did not measure the length because filament D shows a discontinuous spatial distribution.

3.1.2. *Velocity structures of the molecular cloud*

Figure 4 shows the velocity structure of ^{12}CO and ^{13}CO in the N159W-North region. Overall, the structure is very complex, with a mixture of various components over a velocity range of 10 km s^{-1}. One of the outstanding features is that the north side is redshifted, while the south side is blueshifted. This trend is quantitatively similar to the N159E-Papillon and N159W-South regions (Papers I and II). We extracted position-velocity (PV) diagrams across the two YSO locations to examine the velocity structure around them in more detail (Figure 4c,d). The velocity is distributed discontinuously with a boundary around the offset axis of ∼3 pc. As one can see, there are velocity width enhancements toward the two YSO positions. A particular feature seen in ^{12}CO is the outflow contribution from the YSOs (Sect. 3.2). Although the outflow itself likely contributes only a few × 0.1 pc, there is also a V-shaped structure around YSO-N2 on the PV diagram over ∼1 pc. This feature may represent a cloud with multiple velocity components interacting with each other (see discussion in Sect. 4.2).

3.2. *Millimeter continuum sources and molecular outflow*

Figure 5 shows the 1.3 mm continuum distributions in the N159W-North region. We focus on the stronger than 5σ emission within the 3σ contour, and we find that there are five spatially well-separated entities. We labeled them as MMS-1, -2, -3, -4, and -5 (see rectangles in Figure 5). MMS-1–5 have a projected distance of 1–2 pc from the nearest neighbors. The largest/brightest one is MMS-1, coinciding with YSO-N1. Indebetouw et al. (2004) detected 3 cm continuum emission toward this source, and our ALMA observations of H30α show a similar spatial extension to the 1.3 mm emission. These results demonstrate that the free-free emission from ionized material largely contribute to the continuum emission from MMS-1. The N159E-Papillon region shows a similar 1.3 mm continuum structure whose size scale is ∼5″ (Paper I; see also Figure 14b), but it is visible in the optical Hα band, unlike MMS-1 in N159W-North. The Papillon nebula is more evolved than N159W-North MMS-1 and/or one of the complex velocity components in the foreground hides the ionized gas. In fact, a part of 1.3 mm emission in MMS-1 overlaps with the C^{18}O distribution (see Figure 6a). In the other 1.3 mm sources, the previous measurements, such as longer wavelength radio observations, and hydrogen recombination lines, did not find any indication of ionized material. The thermal dust emission is the main contributor, which is consistent with that of the continuum emission spatially correlates with C^{18}O well (see Sect. 3.3).

Our visual inspection of MMS-2 and MMS-4 revealed six and two local peaks, respectively (Figure 5a). We defined their boundary as 50% intensity in each peak, including MMS-3, and -5, to estimate the physical quantities (Table 2). Although multiple peaks can be also identified in MMS-1, we treat it as a single continuous source in this paper, since a large free-free contribution makes it difficult for us to estimate the physical quantities of thermal component with the 1.3 mm measurement alone. The flux, $F_{\rm 1.3mm}^{\rm MMS}$, is converted to molecular gas mass, $M_{\rm MMS} = D^2 F_{\rm 1.3mm}^{\rm MMS}/R_{\rm dg}\kappa_{\rm 1.3mm}B(T_{\rm d})$, where D is the distance to the source, $R_{\rm dg}$ is the dust-to-gas mass ratio, $\kappa_{\rm 1.3mm}$ is the absorption coefficient per unit dust mass at 1.3 mm, and $B(T_{\rm d})$ is the Planck function at a dust temperature

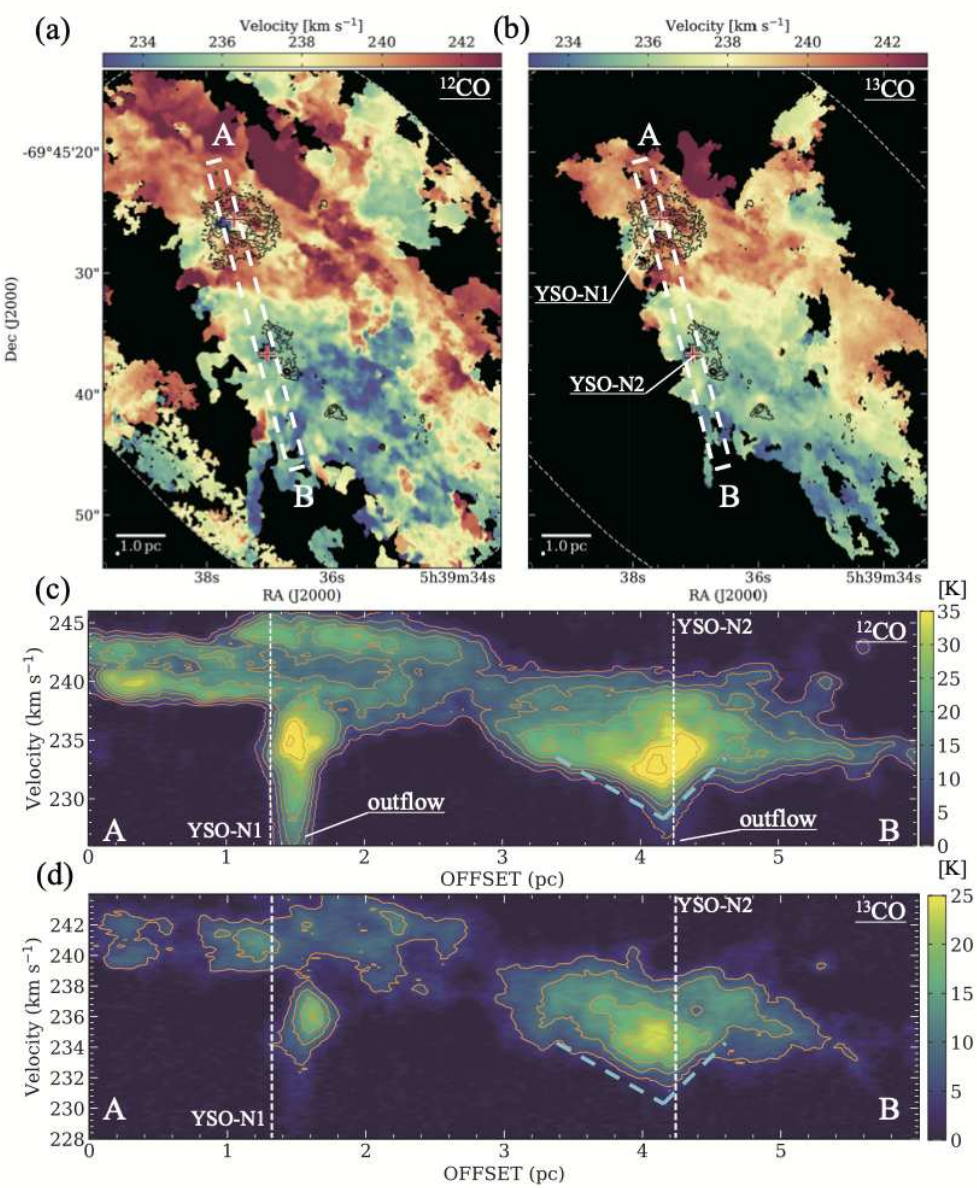

Figure 4. (a) The color-scale image illustrates the first-moment intensity-weighted velocity map of ^{12}CO(J = 2–1). The white ellipse in the lower-left corner gives the angular resolution, 0.″27 × 0.″23. The portion of a white dashed ellipse indicates where the mosaic sensitivity falls to 50%. The rectangle defined by the white thick line marks the extracted region to make the position-velocity diagram in panels (c,d). The black contours show the 1.3 mm continuum image. The lowest contour and subsequent steps are 0.1 mJy beam^{-1}. The red crosses denote positions of two YSOs (Chen et al. 2010). (b) Same as (a) but for the ^{13}CO(J = 2–1). (c) The color-scale and orange contours show the ^{12}CO(J = 2–1) position-velocity diagram along the rectangle shown in panel (a) The contour levels are [5,10,15,20,25,30,35,40] K. The two dashed lines represent the positions of YSO-N1 and -N2. (d) Same as (c) but for ^{13}CO(J = 2–1). The contour levels are [5,10,15,20] K.

$T_{\rm d}$. Our assumptions are following; $R_{\rm dg} = 3.5\times10^{-3}$, and $\kappa_{1.3{\rm mm}} = 1\,{\rm cm^2\,g^{-1}}$ (see, Ossenkopf & Henning 1994; Herrera et al. 2013; Gordon et al. 2014). Assuming that the dust and gas temperatures couple in the dense medium at a core scale (e.g., Young et al. 2004; Ceccarelli et al. 2007), we applied the gas temperature determined from ammonia observations (16 K, Ott et al. 2010) as $T_{\rm d}$. As summarized in Table 2, the peak column density and mass of the sources are as high as (0.4–1)$\times10^{24}$ cm^{-2}, and (0.7–3)$\times10^2\,M_\odot$, respectively.

We investigated the presence or absence of known infrared counterparts in each continuum source to characterize the star formation activities. The Spitzer-based YSO identifications do not have a sufficient angular resolution to determine

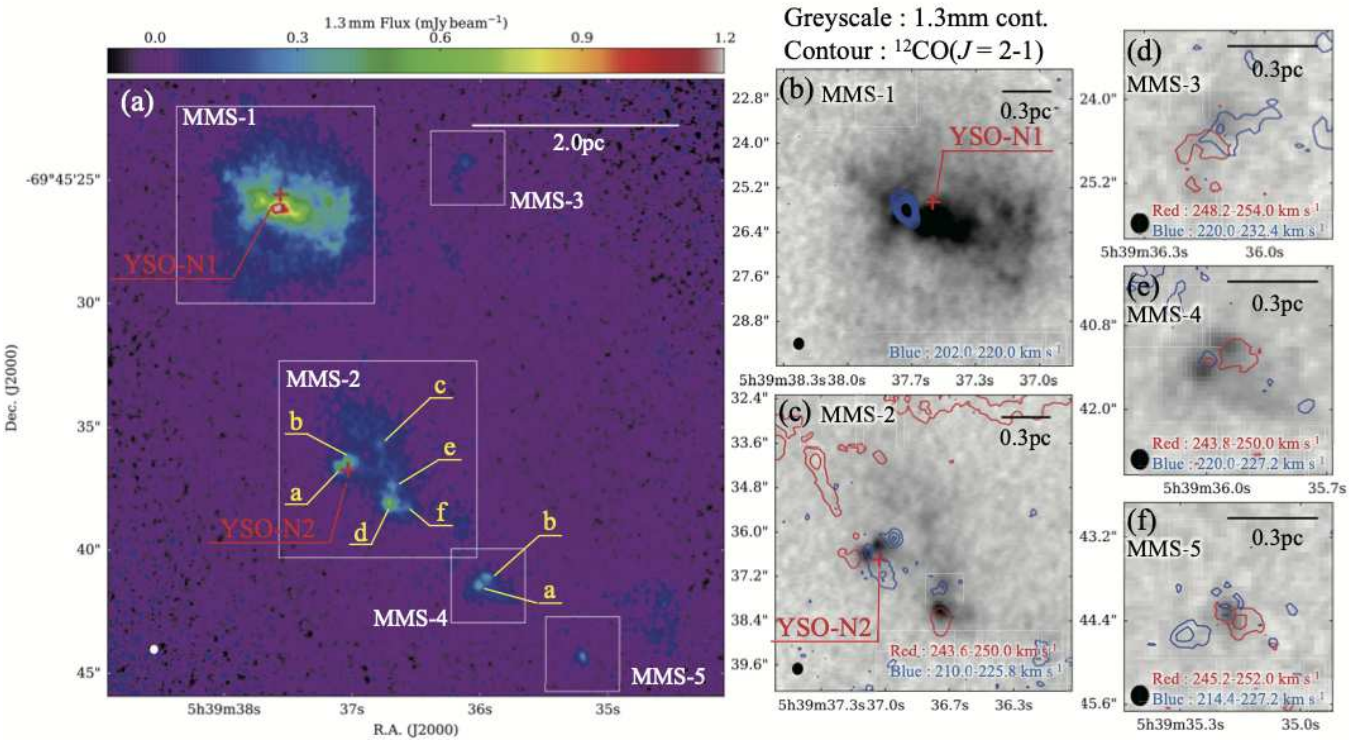

Figure 5. 1.3 mm continuum and ^{12}CO high-velocity emission toward N159W-North. (a) The color-scale image illustrates the 1.3 mm continuum emission. The white ellipse in the lower-left corner gives the beam size of 0.″26 × 0.″23. The red crosses indicate the positions of YSOs (Chen et al. 2010) identified using the Spitzer data with an aperture radius of 3.″6. (b–f) Enlarged views of each millimeter source. Red and blue contours shows the redshifted and blueshifted high-velocity emission of ^{12}CO(J = 2–1). The integrated velocity range are given in lower right corners in each panel. We arbitrarily adjusted the contour level to emphasize the weaker components in each target. Black ellipses in each lower left corner show the beam size of 1.3 mm continuum.

which sources, MMS-2a and -2b, are brighter in the mid-infrared wavelength. Bernard et al. (2016) performed high-resolution near-infrared observations using the VLT (Very Large Telescope) at an angular resolution of ∼0.″1 with a sensitivity of 21.85 mag in K_s. We independently verified the positional accuracy of the VLT detected sources using the GAIA DR2 catalog (Bailer-Jones et al. 2018). MMS-2a is visible in K_s band, while MMS-2b was not detected. MMS-2d is detected in K_s, but the position is slightly (∼0.″1) shifted to the east direction from the continuum peak. According to Bernard et al. (2016), the source is categorized as a YSO candidate based on the color-magnitude diagram. Figure 6b visualizes the presence/absence of the infrared sources in MMS-2. In the other continuum sources, we could not find any known infrared counterparts.

Our previous studies (Papers I and II) discovered molecular outflows in ^{12}CO at some of the 1.3 mm continuum sources in the N159E-Papillon and W-South regions. The new ALMA measurements enable us to make a powerful guide map additionally searching for star formation activity in infrared quiescent sources (see also some Galactic studies on infrared dark clouds (IRDC), e.g., Kong et al. 2019). In the same manner, described in Paper II, we manually searched for high-velocity wing emission more than ∼10 km s^{-1} away from the systemic velocity determined by the ^{13}CO spectra at each continuum source. Figures 5b–f present the spatial distributions of ^{12}CO high-velocity emission (see also the spectra of Figure 12 in Appendix C). We conclude that the high-velocity emission is most likely due to molecular outflows from embedded protostellar object(s) inside the continuum sources. The high-resolution ^{12}CO data reveals the outflow population in this region for the first time, except for the monopolar one at YSO-N1 inside MMS-1, which was already reported in the previous lower resolution ALMA study (Fukui et al. 2015). The characteristics of the outflows are comparable to those in N159E-Papillon/N159W-South (Papers I and II); the typical size and maximum velocity of the flows are ∼0.2 pc, and ∼20 km s^{-1}, respectively. Only one exception is the blueshifted emission in MMS-1 whose maximum velocity is not captured by the current observing setting in the Cycle 4 data.

Table 2. Physical quantities of 1.3 mm continuum sources in N159W-North

Name	α (J2000.0)[a]	δ(J2000.0)[a]	$F_{1.3\mathrm{mm}}^{\mathrm{max}}$ [mJy beam^{-1}]	$F_{1.3\mathrm{mm}}^{\mathrm{MMS}}$ [mJy][b]	N_{peak}[cm^{-2}][c]	M_{MMS} [$M_{\odot}$][d]	I.R. source
MMS-1[e]	05:39:37.55	-69:45:26.11	1.36	12.2	...[e]	...[e]	Y
MMS-2a	05:39:37.09	-69:45:36.56	0.56	0.8	1×10^{24}	1×10^{2}	Y
MMS-2b	05:39:37.03	-69:45:36.40	0.53	1.1	1×10^{24}	2×10^{2}	N
MMS-2c	05:39:36.78	-69:45:35.67	0.24	1.1	5×10^{23}	2×10^{2}	N
MMS-2d	05:39:36.71	-69:45:38.09	0.63	2.0	1×10^{24}	3×10^{2}	Y
MMS-2e	05:39:36.68	-69:45:37.39	0.31	1.1	7×10^{23}	2×10^{2}	N
MMS-2f	05:39:36.57	-69:45:38.24	0.25	0.5	5×10^{23}	1×10^{2}	N
MMS-3	05:39:36.13	-69:45:24.31	0.20	0.4	4×10^{23}	7×10^{1}	N
MMS-4a	05:39:36.00	-69:45:41.42	0.39	0.7	8×10^{23}	1×10^{2}	N
MMS-4b	05:39:35.94	-69:45:41.10	0.34	0.7	7×10^{23}	1×10^{2}	N
MMS-5	05:39:35.19	-69:45:24.31	0.32	0.4	7×10^{23}	7×10^{1}	N

[a] Peak sky coordinate in 1.3 mm.

[b] Flux of the 1.3 mm continuum emission above ∼50% intensity level from each peak.

[c] H_2 column density at each peak.

[d] Total gas mass within the same region to measure $F_{1.3\mathrm{mm}}^{\mathrm{MMS}}$.

[e] MMS-1 shows multiple peaks, but we treated it as a single source and did not derive the column denisty and mass, because there is a large free-free contamination (see the text).

An alternative ALMA project using the CO(3–2) line (K., Tanaka et al. in prep.) detected more than ∼60 km s^{-1} emission in this source.

Among the 1.3 mm continuum sources, MMS-2c, e, and f do not harbor either infrared nor ^{12}CO high-velocity emission, indicating that these sources are purely starless at least in the high-mass regime (Figure 6b). The inferred gas mass is as massive as ∼100 $M_{\odot}$ (see Table 2). Although some Galactic observations using ALMA discovered similar sources in high-mass star-forming regions (e.g., Kong et al. 2017; Molet et al. 2019; Zhang et al. 2021), our finding is the first discovery of starless massive core candidates in extragalactic studies at less than 0.1 pc resolution.

3.3. *Dense molecular gas traced by $C^{18}O$ in N159W-North*

Figure 6a illustrates the C^{18}O integrated intensity maps in the N159W-North region. The emitting regions of the rare isotope are more spatially compact than those of ^{12}CO and ^{13}CO, and have good spatial correlation with the millimeter sources. These features clearly demonstrate that the C^{18}O traces a high density inside of the molecular cloud. We defined the dust and gas rich region as "main ridge" where we detect both the 1.3 mm and C^{18}O emission and the ^{13}CO integrated intensity map enables to enclose the dense condensations with a single contour level of ∼70 K km s^{-1}. The maximum integrated intensity is ∼12 K km s^{-1} around MMS-2c, which is the most massive starless source inferred from the 1.3 mm measurement (Sect. 3.2). In the MMS-1, the C^{18}O emission is relatively weak compared to that in MMS-2, and the extended 1.3 mm component is not bright in C^{18}O. This is because the dense gas around the high-mass protostellar object, YSO-N1, is beginning to dissipate, and the extended 1.3 mm emission is mainly arising from the ionized gas as described in Sect. 3.2.

We quantitively characterize the C^{18}O clumps in the N159E/W region (Table 3, see also Figure 14 in Appendix E). Our assumption to estimate the virial mass, $M_{\mathrm{vir}} = 210 R_{\mathrm{clump}} \Delta v_{\mathrm{clump}}^2$, where R_{clump} is the C^{18}O clump radius in parsec and $\Delta v_{\mathrm{clump}}$ is the FWHM of the line profile in km s^{-1}, are a uniform density inside the clump and ignoring the magnetic field contribution. To estimate the luminosity-based H_2 mass using the LTE assumption, we need to apply a conversion factor, i.e., relative abundance, [H_2]/[C^{18}O]. According to Galactic studies (e.g., Frerking et al. 1982), a commonly used value of [H_2]/[C^{18}O] is ∼5.9 $\times10^6$. However, the early single-dish measurements by Johansson et al. (1994) showed that C^{18}O emission in the LMC is quite weak, indicating that [H_2]/[C^{18}O] in the LMC is about 20 times higher than in the Milky Way (MW), ∼1.2 $\times10^8$. We adopted the higher value as the conversion factor to derive the

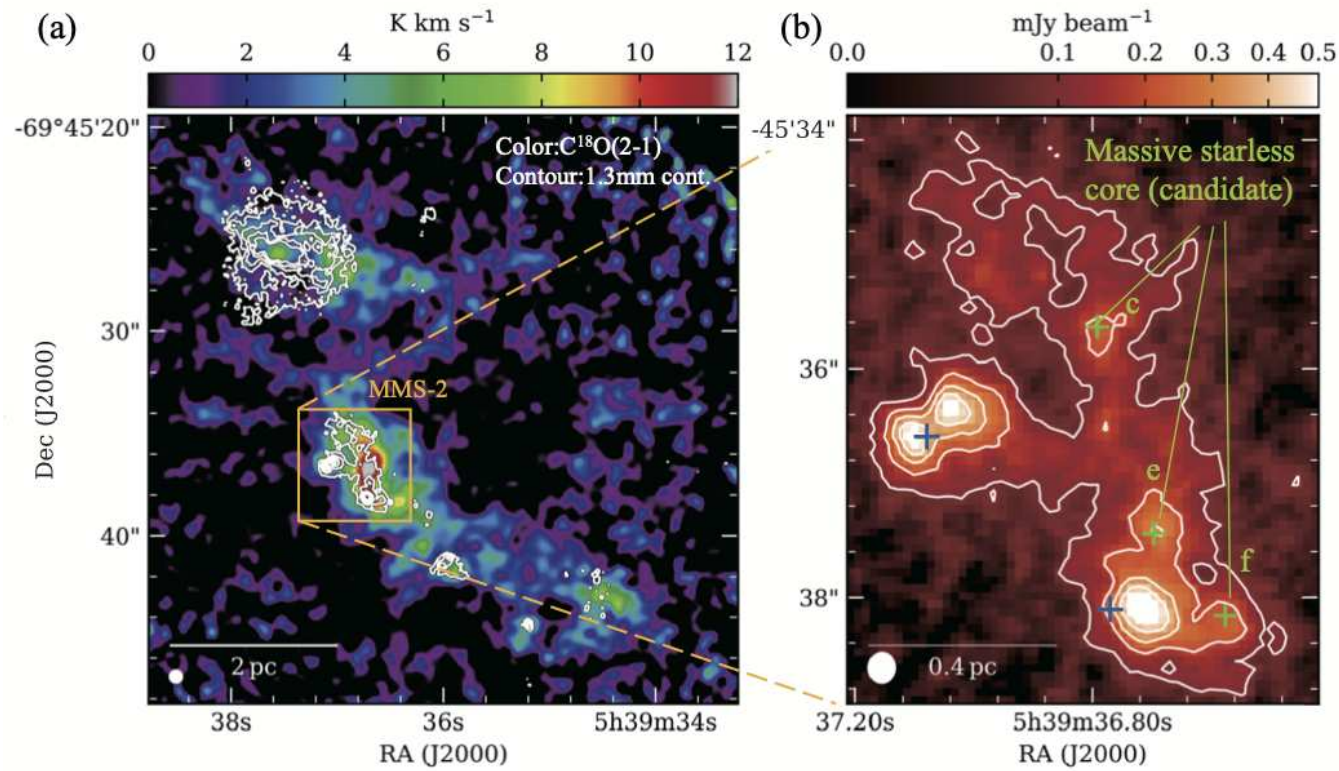

Figure 6. $C^{18}O$ and 1.3mm continuum emission in the main ridge of N159W-North. (a) The color-scale image illustrates the $C^{18}O$ integrated intensity image with an angular resolution of 0.″6. The beam size is shown by the white ellipse in the lower left corner. The contours shows the 1.3 mm continuum emission. The lowest and subsequent contour steps are 0.1 mJy beam^{-1}. (b) The color-scale image and contours shows an enlarged view of the 1.3 mm continuum emission toward MMS-2. The contour levels are the same as panel (a). The white ellipse at the lower left corner shows the beam size of 0.″26 × 0.″23. The blue and green crosses represent positions of the infrared and starless sources, respectively.

LTE mass. The resulting masses are one order of magnitude larger than the virial mass (Table 3), which is typical for such a dense, gravitationally bound system (see also Nayak et al. 2018). The current observational evidence suggests that the main ridge in N159W-North and its subregions have dense gas, whose density and total masses are $\sim 10^5$ cm^{-3} and $\gtrsim 10^4\,M_\odot$, respectively.

3.4. *A comprehensive CO view around/in the N159W-North region*

Figure 7a illustrates the CO(J = 1–0) peak brightness temperature map. The field coverage is the widest among the N159W ALMA studies using CO and its isotope lines with a sub-pc resolution. Note that we arbitrarily extracted a velocity range of 234.7–239.5 km s^{-1} to highlight the N159W-North related structures in Figure 7a. The velocity-channel map is presented in Figure 13 of Appendix D.

As one can see, there are at least two elongated or filamentary features intersecting around the main ridge region as indicated by the triangle in Figure 7a. The total projected lengths of the western and eastern clouds are ∼20 pc and ∼30 pc, respectively. Although their central velocities differ from each other by a few km s^{-1}, they are spatially connected via the main ridge, making a single large system. We call this chain of features "conical cloud" hereafter. These characteristics qualitatively resemble those of the V-shaped filament in the N159W-South region (Fukui et al. 2015; Paper II). The southern tip of the conical cloud, which roughly lies to the Cycle 4 field coverage, has CO peak brightness temperature of $\gtrsim$30 K. Compared to the entire conical cloud, the temperature rises across the main ridge region, not only the internal subregion, the warm side introduced in Sect. 3.1.

The total CO(1–0) luminosity of the conical cloud is 3.7×10^3 K km s^{-1} pc^2, corresponding to $\sim 1.6\times10^5\,M_\odot$ if we assume a CO-to-H_2 conversion factor, 5×10^{20} cm^{-2} (K km s^{-1})$^{-1}$ (Hughes et al. 2010). The conical cloud is an order of magnitude more massive than the N159W-South cloud, $\sim 10^4\,M_\odot$ (Paper II). Because the comprehensive single-

Table 3. Physical properties of $C^{18}O$ clumps in N159E/W

Region name	$R_{\rm clump}$ [pc][a]	$\Delta v_{\rm clump}$ [km s^{-1}][b]	$V_{\rm cent}$ [km s^{-1}][b]	$M_{\rm vir}$ [$M_\odot$][c]	$M_{\rm LTE}$ [$M_\odot$][d]
MMS-1	0.63	5.9	239.9	5×10^3	1×10^4
MMS-2	0.71	4.6	235.6	3×10^3	2×10^4
MMS-4	0.36	2.6	236.2	5×10^2	1×10^3
MMS-5	0.31	2.5	235.0	4×10^2	1×10^3
main ridge[e]	···	···	···	···	4×10^4
N159E-Papillon	0.41	3.1	232.4	8×10^2	7×10^3
N159W-South	0.38	4.6	236.1	2×10^3	5×10^3

[a] Radius of a circle having the same area above the $C^{18}O$ integrated intensity of $\sim$4 K km s^{-1}, which corresponds to $\sim5\sigma$ noise level.

[b] Velocity width in FWHM ($\Delta v_{\rm clump}$) and central velocity ($V_{\rm cent}$) of the $C^{18}O$ spectra at the peak sky coordinate in each clump.

[c] Virial mass, $M_{\rm vir} = 210 R_{\rm clump}\Delta v^2_{\rm clump}$ (see the text).

[d] The LTE mass assuming the uniform excitation temperature of 20 K and $[H_2]/[C^{18}O]$ of $\sim1.2\times10^8$ (see the text) within the region having $>5\sigma$ $C^{18}O$ emission.

[e] We defined only the $M_{\rm LTE}$, because the $C^{18}O$ emitting regions are not spatially connected.

dish survey in the LMC shows that the N159W region is the most CO intense spot (see also Sect. 1), the conical cloud is likely one of the largest and brightest structures in this galaxy. Based on the spatial distribution of YSO candidates (Chen et al. 2010), the western part of the observed field (RA(J2000)$\lesssim5^{\rm h}39^{\rm m}30^{\rm s}$) seems quiescent in high- and intermediate-mass star formation, although we see a lot filamentary structure with a strong intensity contrast. The total molecular gas mass of this quiescent region is $\sim1.2\times10^5\,M_\odot$. In summary, about half of the total mass of molecular material is associated with the current high-mass star formation in this observed field.

Figure 7b highlights the characteristic features presented in Sect. 3.1, and 3.2 to guide the positional relationship with each other on the high-resolution CO map.

4. DISCUSSION

4.1. *Dynamical status of the characteristic components*

This section discusses the physical states of the newly discovered features in N159W-North with our ALMA observations described in Sect. 3.

4.1.1. *Filaments traced by ^{12}CO and ^{13}CO*

Several filaments are seen extending from the southern edge of the main ridge (Sect. 3.1.1). They are relatively ordered in the north-south direction and their roots appear to be spatially attached to the protostellar systems in MMS-1 and MMS-2. We discuss here the dynamical state (stability) of the filaments to infer a possible fate. As shown in Sect. 3.1.1, the virial line mass of filaments is somewhat larger than those of the ^{12}CO luminosity mass. If we ignore the stabilizing effect by magnetic force, the filaments are not gravitationally stable objects. In this case, the filaments can be dissipated within a turbulent crossing time, which is an order of $\sim10^5$ yr $= W_{\rm fil}/\sigma_v$, where $W_{\rm fil}$ is the typical width of filament ($\sim$0.1–0.2 pc). In fact, the current star formation is inactive in all of the filaments except for their junctions with the millimeter sources. Among them, filament D has the weakest and shows the discontinuous ^{12}CO distribution (Figure 3(a3)), suggesting that this filament is the oldest one and is currently in the process of dissipating.

We discuss possible formation scenarios of the filaments in the N159W-North region. The filaments spatially connect to the protostellar source, and thus they are likely related to the star formation activity. Schneider et al. (2010) found similar ^{13}CO filaments toward the most massive clump in the Galactic Cygnus X DR21 region. The morphological features and physical properties, such as mass ($M\sim2600\,M_\odot$) and length ($L\sim5$ pc), are very similar to N159W-North. The authors interpreted this as filaments falling onto the central ridge due to the global collapse. However, this interpretation is not necessarily supported by gas kinematic features, e.g., accelerated motion toward the star-forming main ridge. A robust common feature of the filaments in the N159W-North regions is that they are distributed only on one side of the main ridge, suggesting the existence of an asymmetric gas flow through the main ridges. The

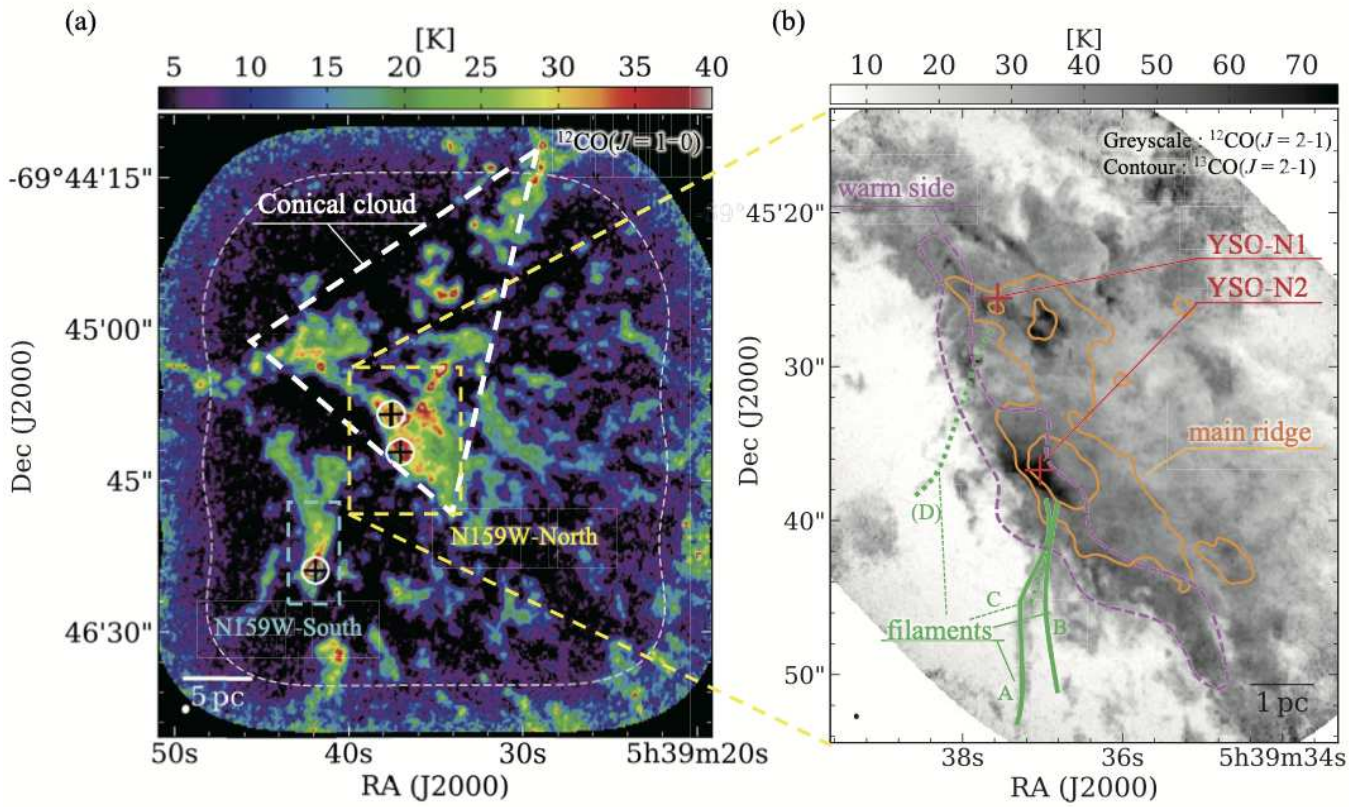

Figure 7. Multi-spatial-scale molecular gas view around the N159W-North region. (a) The color-scale image illustrates the ^{12}CO(J = 1–0) peak brightness temperature map extracted from a velocity range of 234.7–239.5 km s^{-1}. The white dashed contours indicates where the mosaic sensitivity falls to 50%. The white ellipse in the lower-left corner gives the angular resolution, 2.″2 × 1.″8. The region determined by white dashed triangle represent the CO emitting regions defined as the conical cloud. The yellow and cyan dashed rectangles indicate the N159W-North and -South regions studied in this work and Paper II, respectively. Black crosses with white circles indicate positions of YSO candidates (Chen et al. 2010) within the Cycle 4 observed field. (b) An explanatory map of distinct features (see the text) in the N159W-North region on the high-resolution ^{12}CO(J = 2–1) peak brightness temperature image, which is the same as the color-scale image in Figure 2a. The black ellipse in the lower-left corner gives the angular resolution, 0.″27 × 0.″23. Orange contour shows a smoothed ^{13}CO(J = 2–1) velocity-integrated intensity image with contour levels of 70 and 140 K km s^{-1}.

warm side nature can be explained by the past shock wave event in this region (see Sect. 4.1.2), and thus we propose that an extensive gas flow penetrates the N159W-North main ridge and promotes the high-mass star formation with remarkable filaments. We will discuss this possibility further in Sect. 4.2.

4.1.2. *Warm side*

We found that the peak brightness temperature of ^{12}CO at the southeast edge of the main ridge is remarkably high ($\gtrsim$50 K) compared to the typical value ($\sim$30 K) of this region, indicating that something is contributing to the heating. The probable reasons are (case 1) external radiation field and cosmic ray heating, (case 2a) shock heating in the turbulent material within the cloud, and/or (case 2b) shock heating due to external gas compression. Lee et al. (2016) obtained multi-line CO transitions up to J = 12–11 in the N159W region using Herschel Space Observatory and ground-based telescopes, and estimated the molecular gas kinematic temperature of >100 K and density of $\sim 10^3$ cm^{-3} on $\sim$10 pc scale. Their modeling showed that case 1 is unlikely to produce the warm environment, and instead, suggested that low-velocity C-type shocks (case 2a and/or 2b) with $\sim$10 km s^{-1} appear to be more plausible. Our narrow field coverage and high-resolution observations highlight the detection region of the rare isotopes of CO, and we are selectively looking only at denser and colder regions than the Lee et al. (2016) study. However, the origin of the cloud nature can still be understood in the same context, because there is no significant external heating source near the ALMA observed region too. For case 2a, Tokuda et al. (2018) actually found warm CO (30–60 K) filamentary

components in a turbulent low-mass star-forming dense core in Taurus. However, the physical scale of the gas is quite small as 1000 au that our present study could not resolve, and shock heating with internal turbulence is expected to realize a more stochastic temperature distribution, instead of asymmetric heating region over several pc as seen in N159W-North. We conclude that mechanical heating due to an external gas colliding flow (case 2b) is probable.

4.1.3. *Dense clumps in the main ridge traced by $C^{18}O$ and 1.3 mm and star-formation activities therein*

We found that the molecular mass of the main ridge of N159W-North and the most massive inside clump exceeds $10^4\,M_\odot$, despite their compactness with a size of less than a few parsecs. Such a massive clump, which is not frequently discovered in the MW disk region, agrees with the mass and size requirements to evolve into a young massive cluster (e.g., Longmore et al. 2014). Table 4 lists several massive clumps studied in the Local Group of galaxies (MW, LMC, and M33). Note that a large-scale survey of molecular gas has been conducted at the SMC, but such a massive clump has not been discovered yet (Tokuda et al. 2021). The mass estimates based on the thermal dust emission and/or molecular line emission are subject to a factor of two or three uncertainties due to methodological differences and systematic errors arising from, e.g., dust properties and molecular abundance. Therefore, we cannot immediately conclude that our characterization of the N159W-North main ridge is the most massive in the Local Group, but it is certainly one of the most massive. The N113 region also has very massive clumps, and thus it could be one of the top contenders in the LMC. However, because this source was not detected in the ATCA NH_3 observations (Ott et al. 2010), the dense gas fraction is likely smaller than that of the N159W-North main ridge.

Table 4. Physical properties of cluster-forming massive clumps in the Local Group

Clump Name	Hosting Galaxy	Size[a] [pc]	M_{H_2} [$M_\odot$]	$N_{H_2}^{peak}$ [cm^{-2}]	$n_{H_2}^{ave}$ [b] [cm^{-3}]	Beam [pc]	Tracers	References[c]
N159W-N main ridge[d]	LMC	1.1×3.3	$\sim7\times10^4$	$\sim1\times10^{24}$	$\sim1.0\times10^5$	~0.1	$^{13}CO/C^{18}O$/1.3 mm	This work
MMS-2 [e]		~1.5	$\sim2\times10^4$		$\sim2\times10^5$		$C^{18}O$/1.3 mm	
N113 Region B	LMC	1.2×2.7	$\sim2\times10^4$	$\sim9\times10^{23}$	$\sim9\times10^4$	~0.2	$^{13}CO/C^{18}O$/1.3 mm	[1]
W43 MM1	MW	3.9×2.0	$\sim2\times10^4$	$\sim3\times10^{23}$	$\sim4\times10^4$	~0.5	$C^{18}O$/1.3 mm	[2,3,4]
W49-N		~4	$\sim5\times10^4$	$\sim2\times10^{24}$	$\sim2\times10^4$	~0.1	$^{13}CO/C^{18}O$	[5]
W51 G49.5−0.4		~2.2	$(1–2)\times10^4$	$\sim4\times10^{23}$	$(3–5)\times10^4$	~0.5	$C^{18}O$	[6]
Cygnus X DR21		$\sim4\times1$	$\sim3\times10^4$	$\sim5\times10^{23}$	$\sim10^5$	~0.2	$^{13}CO/N_2H^+$	[7,8]
NGC 604 MMS-1	M33	2.9×1.9	$\sim5\times10^4$	···	$\sim2\times10^4$	$\sim2\times1$	$C^{18}O$/1.3 mm	[9]
GMC-16 MMS		2.2×1.1	$\sim2\times10^4$	···	$\sim2\times10^4$	$\sim2\times1$	$C^{18}O$/1.3 mm	[10]

[a] Projected length of major and minor axes or size in diameter.

[b] Averaged density assuming the uniform, spherical geometry.

[c] References: [1]We retrieved an ALMA archival data (2015.1.01388, see also Sewiło et al. 2018) of CO and its isotope lines at 1.3 mm wavelength (Nishioka et al. in prep.) and applied the same mass estimation method as in N159W-North.; [2]Motte et al. (2003); [3]Louvet et al. (2014); [4]Kohno et al. (2021); [5]Galván-Madrid et al. (2013); [6]Fujita et al. (2021); [7]Schneider et al. (2010); [8]Dobashi et al. (2019); [9]Muraoka et al. (2020); [10]Tokuda et al. (2020)

[d] The parameters are determined by the ^{13}CO intense region as indicated with the orange contours in Figure 7b.

[e] This source is part of the main ridge. The physical properties are the same as those in Tables 2 and 3.

4.2. *Colliding flows promoting the protocluster formation in N159W-North*

We summarize the features described in Sect. 3 and the possibilities discussed in Sect. 4.1. The cluster forming N159W-North main ridge resides at the apex of a conical-shaped structure traced by the CO(1-0) emission (Sect. 3.4). The presence of several southward filaments from the main ridge, together with the warm side features, suggests that a north-south penetrating colliding flow may have triggered the formation of a massive clump.

We compare these features with a molecular cloud collision model. Many, if not all, of these qualitative characteristics, are explained by the results of numerical simulation of molecular cloud collision by Inoue et al. (2018). They simulated

that a small cloud collided with a larger cloud with a density of $10^3\,\mathrm{cm}^{-3}$ at a relative velocity of $10\,\mathrm{km\,s}^{-1}$ by solving isothermal magnetohydrodynamic (MHD) equations with self-gravity. Generally, a gas clump colliding with the larger cloud is decelerated once it interacts or sweeps up the same amount of the larger cloud gas. Since turbulence creates many dense clumps in the small cloud, some dense clumps go beyond the arc-like structure. Figure 8 summarizes such phenomenon schematically, and we call the penetrated filamentary feature "funnel-type flow". In the N159W-North region, the conical cloud and warm side show the shock compression layer, and the main ridge with a mass of $\gtrsim 10^4\,M_\odot$ is supposed to be the product of the colliding event. If the filaments represent funnel-type flows described above, the feature could also be a piece of indirect evidence of a colliding flow.

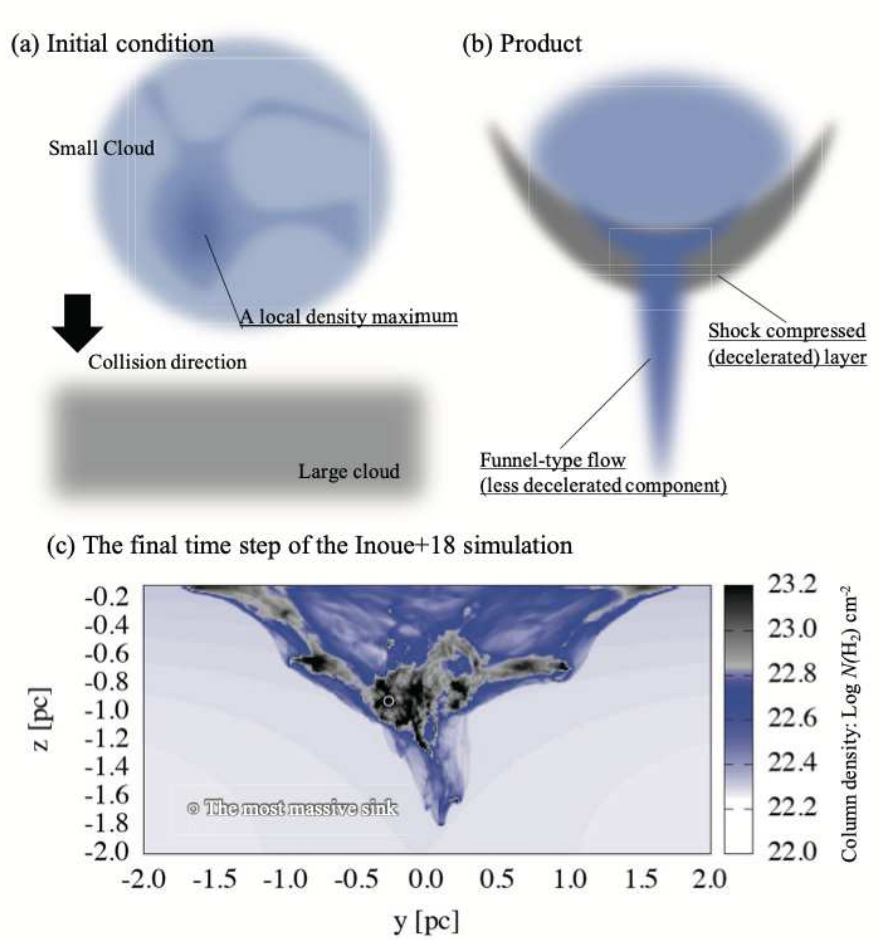

Figure 8. Cloud-cloud collision as a possible formation origin of several distinct features, such as the conical cloud, dense cores, and filaments, in the N159W-North region. Panels (a) and (b) schematically illustrate the initial condition and compressed product after the collision, respectively. (c) The final time step of the MHD simulation by Inoue et al. (2018).

We caveat the discrepancy between our observations and the simulation by Inoue et al. (2018). The N159W-North system is heavier and larger than that in the simulation. Although it is beyond the scope of this paper to perform an optimized calculation for N159W-North, we expect to see further massive clumps with multiple funnel-type flows, if we perform a colliding flow simulation with a higher mass initial condition, because the hydrodynamic phenomenon is basically scale-free.

We presented the morphological features, temperature distribution, and total mass of the dense clump as indirect evidence for molecular cloud interaction, but the velocity analysis enables us to find additional relevant characteristics (Sect. 3.1.2). Paper I shows that the molecular cloud in the N159W-South region has V-shaped structures around protostellar objects on PV diagrams. This feature was originally designed based on numerical simulation reproducing molecular cloud collision phenomena (Takahira et al. 2014 and the subsequent synthetic observations in CO emission

Torii et al. 2017; Fukui et al. 2018). In N159W-North, the V-shaped structure is more prominent around YSO-N2, while the same feature around YSO-N2 is less distinct (see Figure 4) possibly due to the molecular gas ionization (see Sect. 3.2).

4.3. *High-mass star formation across the N159E/W region: an updated view of the synchronized massive cluster formation*

We discuss the massive cluster formation throughout the N159E/W regions by combining current knowledge obtained with molecular and atomic gas observations. Paper I and Paper II found that the massive protostars in N159E-Papillon and N159W-South, respectively, are accompanied by filamentary molecular clouds with their line mass of 300–1000 $M_\odot$ pc^{-1}. Although these two filamentary systems are separated by about 50 pc in the sky, their physical and morphological features are quite similar, suggesting the formation of filaments and massive protostars simultaneously on the order of 0.1 Myr. Papers I and II proposed that the trigger for these events could be the H I colliding flow with a velocity of 50–100 km s^{-1} from the northern direction driven by the last close encounter with the Small Magellanic Cloud ∼2 Gyr ago (Fukui et al. 2017; Tsuge et al. 2019).

Since the newly revealed N159W-North system has a very similar head-tailed filamentary molecular cloud, it is possible that we can interpret its formation scenario in the same context. Figure 9 shows our updated colliding flow star formation scenario, "teardrops inflow model" in the N159 region. In this scenario, the H I gas flow containing multiple dense spots interacts with a pre-existing GMC. Locally, this event can be regarded as a collision between large and small clouds, resulting in the morphological and dynamical features described in Sect. 4.2. N159E-Papillon and N159W-South are impacted by relatively low-mass blobs, while a larger one impacts the N159W-North region, producing a 30 pc scale compression layer. This scenario potentially explains multiple generations of high-mass star formation of N159E/W. N159E already started the main star formation activities 3-4 Myr ago with its numerous O and early B optically-visible stars, except for the above-mentioned young Papillon region, while N159W just started its main episode with mostly massive YSOs (Chen et al. 2010). In this line of thought, assuming that the two regions were in the same pre-existing GMC and only N159E was actively star-forming earlier, the H I dense blob seems likely to be the main contributor to forming many massive cores, i.e., the YMC progenitor, especially in N159W.

Numerical simulations by Maeda et al. (2021) demonstrated ∼10^4 $M_\odot$ massive clump formation driven by a large-scale H I gas flow that mimics galactic interactions. Abe et al. (2021) showed that fast (>10 km s^{-1}) gas flow is more favorable for massive filament formation with a line mass of >100 $M_\odot$ pc^{-1}. From observational perspectives, recent ALMA studies in M33 also found massive filaments with high-mass cluster formation associated with galaxy-galaxy interactions and other galaxy-scale gas motions related to a spiral arm (Tokuda et al. 2020; Muraoka et al. 2020). Galactic high-resolution, large-scale molecular gas surveys toward active cluster-forming regions listed in Table 4 exclusively show complex velocity structures originated from multiple-gas components (Miyawaki et al. 2009, 2021; Dobashi et al. 2019; Kohno et al. 2021; Fujita et al. 2021). The total mass of their parent clouds exceeds 10^6 $M_\odot$, which is an order of magnitude higher than the typical GMC mass, and thus the collision/coalescence of clouds and/or the large-scale diffuse gas inflow from the surrounding environment likely contribute to the formation of gravitationally bound massive clumps that leads to YMC formation.

In the N159E-Papillon and N159W-South regions, the total filamentary gas and dense gas masses are ∼10^4 $M_\odot$ and ∼10^3 $M_\odot$, respectively, suggesting they may be just medium-sized clusters. On the other hand, in N159W-North, the total gas mass of the large-scale filamentary cloud (conical cloud) and dense gas (main ridge) exceed 10^5 $M_\odot$ and 10^4 $M_\odot$, respectively, indicating that the system grows into a more massive cluster. Fukushima & Yajima (2021) numerically demonstrated that a 10^4 $M_\odot$ molecular cloud packed into a few pc volume is converted into a cluster with a high star formation efficiency because the gravitational potential is stronger than the negative feedback force of the stars formed. This case allows forming a massive cluster with a mass of $\gtrsim 10^4$ $M_\odot$ in the N159W-North region. Furthermore, since a part of the conical cloud with a total mass of ∼10^5 $M_\odot$ is connected to the main ridge, it may grow into a massive cluster comparable to R136 in 30 Dor if the conveyor belt-like gas supply mechanism where gas accretion and star formation occur simultaneously (Longmore et al. 2014; Krumholz & McKee 2020) works in this region.

Although the large-scale H I flow scenario was originally designed to explain the R136 formation (Fukui et al. 2017), the fact that the same flow distributes over a kpc scale motivates us to apply it describing the star formation history in N159. In a reimportation of this context, an ALMA wide-field imaging study found a N159-type conical-shaped molecular filament system around R136 (T. Wong et al. submitted). These observational pieces of evidence may

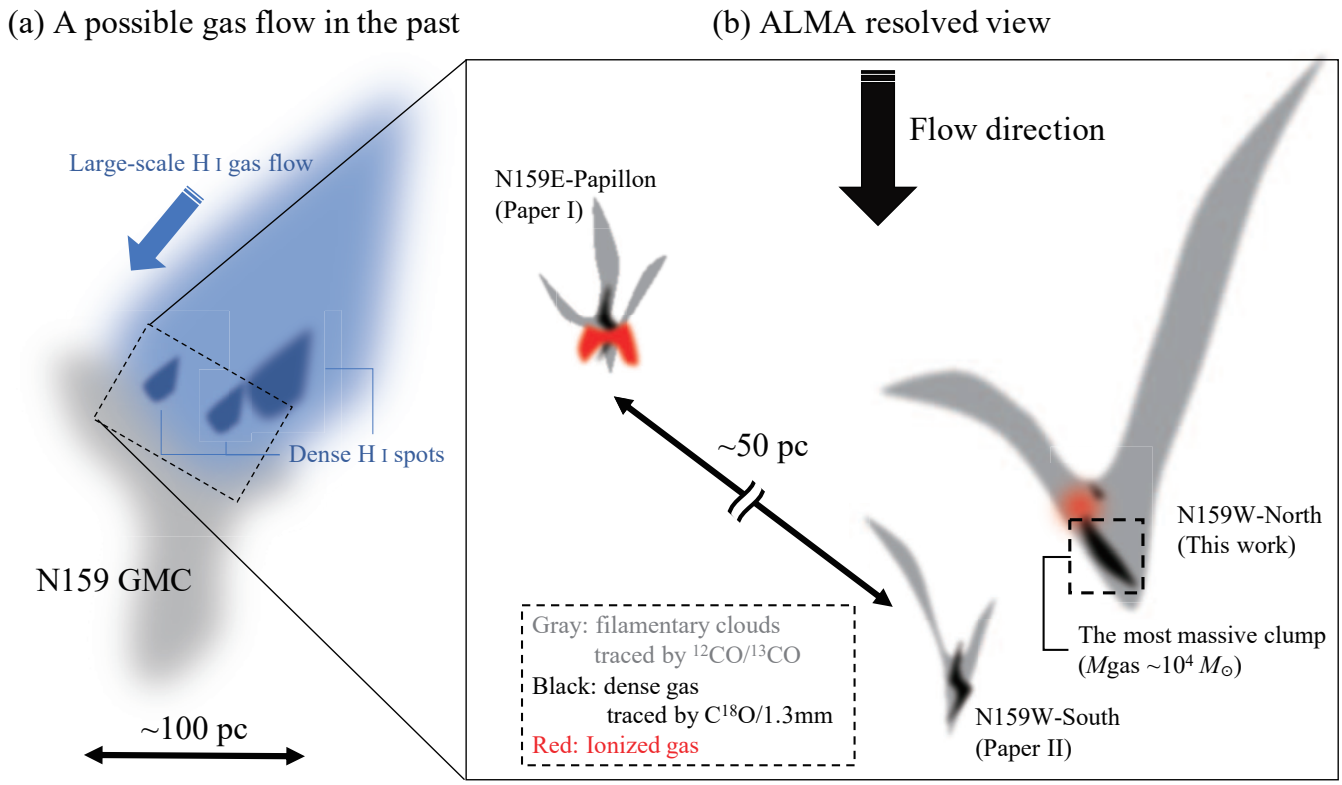

Figure 9. Schematic view of the star formation process in N159E/W motivated by the ALMA studies.

demonstrate that galaxy-scale (H I) gas flows and the subsequent more than a few $\times$ 10 pc scale filament system development are universally responsible for the super star cluster formation that can drive galaxy evolution itself. Since clusters larger than $10^5\,M_\odot$ are only found in a limited number in the Local Group, further searches for similar filament systems in more remote galaxies will help to elucidate the super star cluster formation mechanism in the local universe.

5. CONCLUSIONS

Our ALMA observations revealed a comprehensive molecular gas view of the N159W-North region in the LMC with a high-dynamic spatial range from a few $\times$10 pc to $\lesssim$0.1 pc. The main results and conclusions are summarized as follows:

- The ^{12}CO and ^{13}CO high-resolution data depicted highly complex spatial and velocity structures of the N159W-North molecular cloud. The ^{12}CO brightness temperature is higher than $\sim$30 K throughout the observed region and even higher than $\sim$50 K, especially in the southern side of the cloud. One of the outstanding features is that several filaments, whose length and line masses are a few parsecs and $\gtrsim$100 $M_\odot$ pc^{-1}, extend from high-mass star-forming dense cores toward the southern direction.

- Based on ^{12}CO high-velocity emission, which appears to be of outflow origin, we found five new bright star-forming cores in 1.3 mm continuum emission at the infrared quiescent spots. We also identified $\sim$0.1 pc scale starless cores with a mass of $\sim$100 $M_\odot$, which were not discovered in the previous extragalactic studies. The dense molecular region (main ridge) traced by thermal dust continuum and C^{18}O harbors the above-mentioned proto- and prestellar cores. The total mass of the cluster-forming clump exceeds $10^4\,M_\odot$ despite its compact size of a few pc, making it one of the most massive, dense categories in the Local Group of galaxies.

- The wide-field CO(J = 1–0) map deciphered a head-tailed conical shape feature, whose size scale and total molecular gas mass are $\sim$30 pc and $\sim$2 $\times 10^5\,M_\odot$, respectively. The strong impacts of a cloud-cloud collision

presumably explain the observed large-scale and small-scale subfeatures, such as the warm side nature and filaments in the southern side of the main ridge.

- Combining our current observational understanding of two other regions in N159, E-Papillon (Paper I) and W-South (Paper II), three systems across more than 50 pc show active star formation simultaneously. Massive clumps, especially N159W-North like objects, are highly rare in the Local Group, indicating that a typical galactic environment cannot easily produce YMC precursors. We hypothesize "teardrops inflow model" to explain the synchronized, extreme cluster formation, possibly driven by a quite dynamic, substructured flow induced by a galactic-scale phenomenon.

We would like to thank the anonymous referee for useful comments that improved the manuscript. This paper makes use of the following ALMA data: ADS/ JAO. ALMA#2012.1.00554.S, 2016.1.01173.S, and 2019.1.00915.S. ALMA is a partnership of ESO (representing its member states), NSF (USA) and NINS (Japan), together with NRC (Canada), MOST and ASIAA (Taiwan), and KASI (Republic of Korea), in cooperation with the Republic of Chile. The Joint ALMA Observatory is operated by ESO, AUI/NRAO, and NAOJ. This work was supported by NAOJ ALMA Scientific Research grant Nos. 2016-03B, Grants-in-Aid for Scientific Research (KAKENHI) of Japan Society for the Promotion of Science (JSPS; grant Nos. JP18K13582, JP18H05440, JP21H00049, and JP21K13962), and NSF award 2009624. The National Radio Astronomy Observatoryis a facility of the National Science Foundation operatedunder cooperative agreement by Associated Universities,Inc. The material is based upon work supported by NASA under award number 80GSFC21M0002 (M. S.). Dr. Benoit Neichel kindly provided us the VLT photometric data (Bernard et al. 2016) to compare spatial distributions of the ALMA millimeter continuum and infrared sources.

Software: CASA (v5.6.1; McMullin et al. 2007), Astropy (Astropy Collaboration et al. 2018), APLpy (Robitaille & Bressert 2012)

APPENDIX

A. DATA QUALITIES

Table 5 gives the beam sizes and r.m.s. sensitivities of each molecular line data.

Table 5. Beam Properties and Sensitivities in the molecular line observations

line name	$B_{\rm maj}$ [arcsec]	$B_{\rm min}$ [arcsec]	$B_{\rm P.A.}$ [deg]	r.m.s$_{\rm ch}$ [K][a]	r.m.s$_{\rm i.i.}$ [K km s^{-1}][b]
^{12}CO(J = 2–1)	0.27	0.23	6.1	1.3	1.1
^{13}CO(J = 2–1)	0.28	0.24	5.6	1.4	1.1
C^{18}O(J = 2–1)	0.28	0.24	4.7	1.0	0.9

[a] Noise level of data cube at a velocity resolution of 0.2 km s^{-1}.

[b] Noise level of integrated intensity image over a velocity range of 5 km s^{-1}, which roughly corresponds to the typical line width of the N159W-North cloud.

B. HIGH-RESOLUTION CO CHANNEL MAPS

Figures 10 and 11 show the ^{12}CO(J = 2–1) and ^{13}CO(J = 2–1) channel maps, respectively, with a velocity bin of 2 km s^{-1}.

C. OUTFLOW SPECTRA AND PROPERTIES

Figure 12 shows ^{12}CO spectra with high-velocity wing emission originated from protostellar sources in MMSs. Table 6 lists the outflow properties.

D. LARGE-SCALE CO CHANNEL MAPS

Figure 13 illustrates the velocity channel maps of ^{12}CO(J = 1–0) across the N159W region.

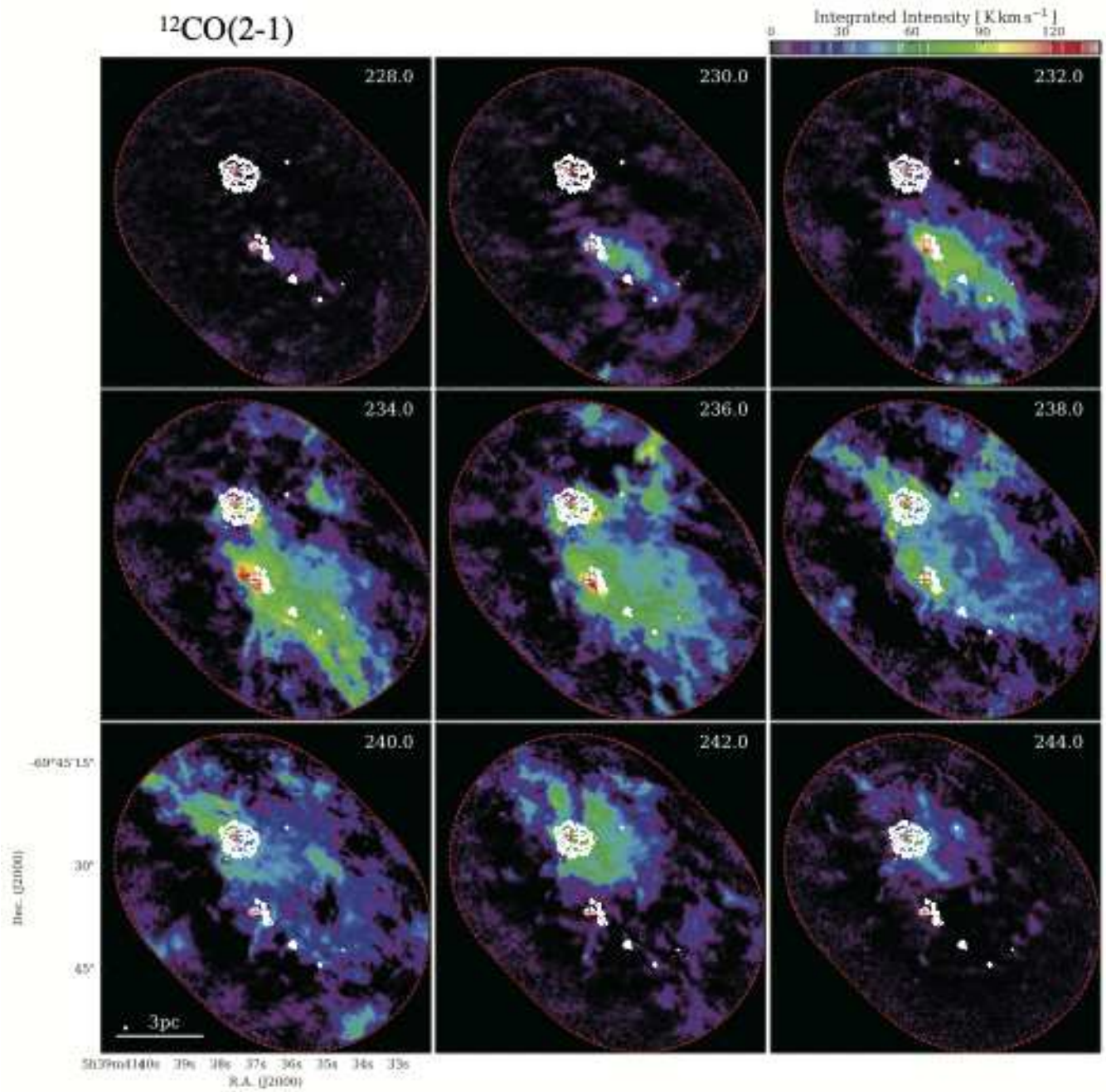

Figure 10. Velocity channel maps of N159W-North in ^{12}CO(J = 2–1). The lowest velocity in unit of km s^{-1} of each panel are given in the upper right corners. The white ellipse in the lower left corner in the lower left panel shows the beam size, 0.″29 × 0.″23, of the ^{12}CO data. Red dotted lines show the field coverage. The white contours show the 1.3 mm continuum emission, same as Figure 2.

E. C^{18}O DENSE CLUMPS TRACED IN THE N159E-PAPILLON AND W-SOUTH REGIONS

We compare the C^{18}O distribution in N159W-North and that in the two dense clumps in N159E-Papillon (Figure 14a) and N159W-South (Figure 14b). Both C^{18}O emitting regions are elongated in the direction along the major axis of the filamentary structures traced in ^{12}CO and ^{13}CO (Figure 1, see also Papers I and II). The emitting region reaches a high-density of $\sim 10^6$ cm^{-3} at maximum in the N159W-South region (Paper I). However, the peak integrated intensities are $\sim$1–2 K which are significantly lower than those in N159W-North. The currently available ALMA surveys (Fukui et al. 2015; Saigo et al. 2017; Papers I and II) detected C^{18}O emission only in these three spots, N159W-North/South, and

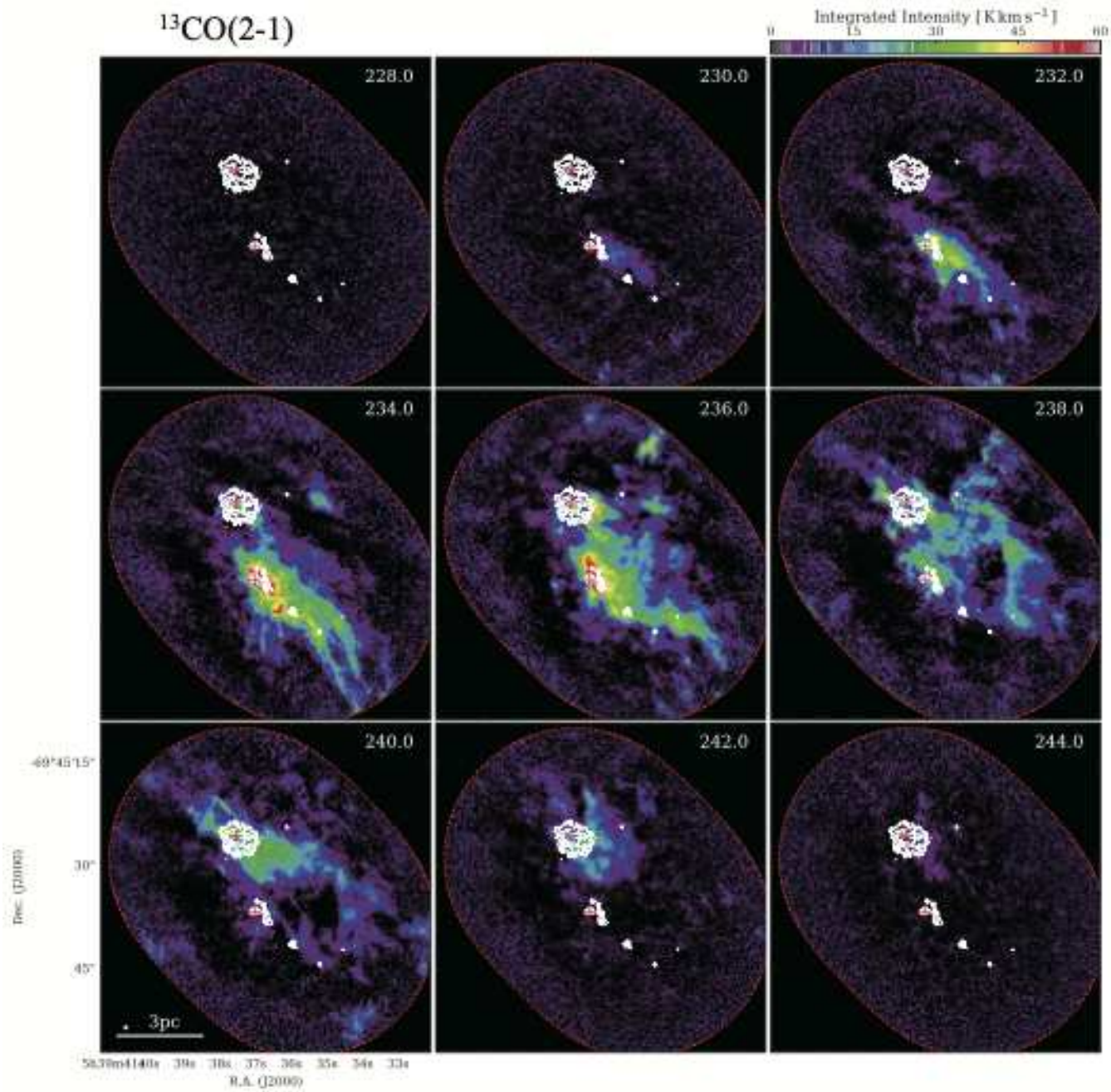

Figure 11. Same as Figure 10, but for ^{13}CO(J = 2–1).

E-Papillon, across the N159E/W region, indicating that the C^{18}O detection itself is highly rare in the LMC (see also the 30 Dor case in Figure 7 of Indebetouw et al. 2013). Among all known C^{18}O emitters, the N159W-North clump is the strongest one in the LMC.

REFERENCES

Abe, D., Inoue, T., Inutsuka, S.-i., & Matsumoto, T. 2021, ApJ, 916, 83, doi: 10.3847/1538-4357/ac07a1

Astropy Collaboration, Price-Whelan, A. M., Sipőcz, B. M., et al. 2018, AJ, 156, 123, doi: 10.3847/1538-3881/aabc4f

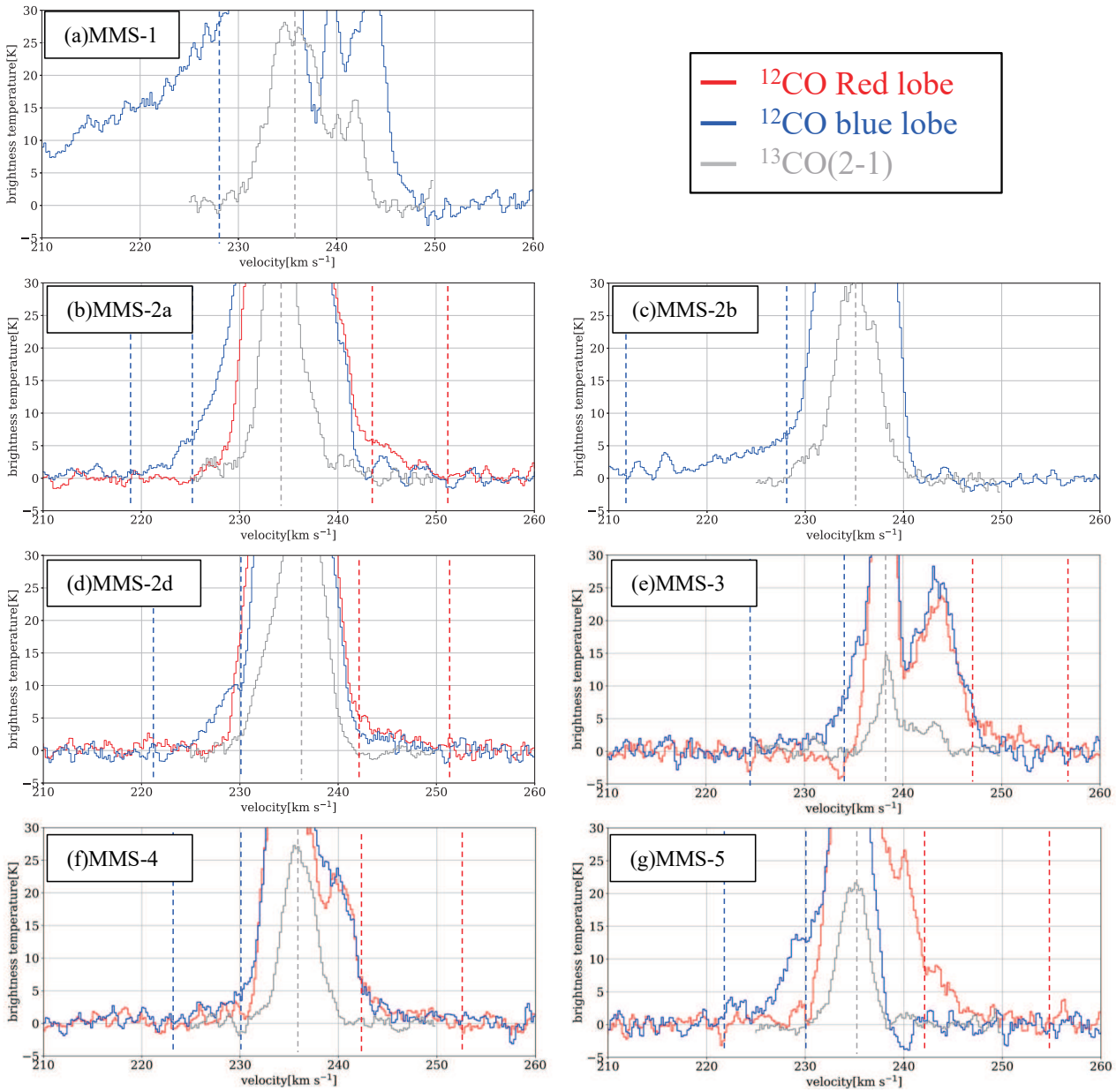

Figure 12. ^{12}CO spectra with high-velocity wing components toward millimeter continuum sources in N159W-North. Red and blue profiles show the ^{12}CO redshifted and blueshifted components, respectively, averaged within the red and blue contours in Figure 5b–f. The red and blue vertical lines indicate the velocity ranges of high-velocity emission (see also Table 6). Gray profiles show ^{13}CO(J = 2–1) spectra at the MMS peaks. Gray dotted vertical lines represent the central velocity determined by Gaussian fitting the ^{13}CO spectra with a single Gaussian profile.

Bailer-Jones, C. A. L., Rybizki, J., Fouesneau, M., Mantelet, G., & Andrae, R. 2018, AJ, 156, 58, doi: 10.3847/1538-3881/aacb21

Balbinot, E., Santiago, B. X., Girardi, L., et al. 2015, Monthly Notices of the Royal Astronomical Society, 449, 1129, doi: 10.1093/mnras/stv356

Bernard, A., Neichel, B., Samal, M. R., et al. 2016, A&A, 592, A77, doi: 10.1051/0004-6361/201628754

Beuther, H., Schilke, P., Sridharan, T. K., et al. 2002, A&A, 383, 892, doi: 10.1051/0004-6361:20011808

Carlson, L. R., Sewilo, M., Meixner, M., Romita, K. A., & Lawton, B. 2012, A&A, 542, A66, doi: 10.1051/0004-6361/201118627

Table 6. Outflow properties associated with millimeter sources (MMSs) in N159W-North

Source	Blue lobe			Red lobe		
Name	$L_{\rm CO}$ [K km s^{-1} pc^2][a]	$v_{\rm max}$ [km s^{-1}][b]	$v_{\rm range}$ [km s^{-1}]	$L_{\rm CO}$ [K km s^{-1} pc^2][a]	$v_{\rm max}$ [km s^{-1}][b]	$v_{\rm range}$ [km s^{-1}]
MMS-1	2.87	>24.8	<210–231	···	···	···
MMS-2a	0.57	15.8	218–225	0.47	18.0	242–252
MMS-2b	0.27	18.0	217–228	···	···	···
MMS-2d	0.05	12.8	223–229	0.70	14.2	242–250
MMS-3	0.21	14.6	224-234	0.48	18.4	247-257
MMS-4	0.04	12.8	223–230	0.27	16.2	243–252
MMS-5	0.23	11.8	223–230	0.20	21.2	243–253

[a]Total CO(J = 2–1) luminosity of outflow lobes above $\sim 3\sigma$ detection.

[b]Maximum radial velocity of outflow lobes with respect to the systemic velocity determined with the ^{13}CO(2–1) spectra.

Ceccarelli, C., Caselli, P., Herbst, E., Tielens, A. G. G. M., & Caux, E. 2007, in Protostars and Planets V, ed. B. Reipurth, D. Jewitt, & K. Keil, 47. https://arxiv.org/abs/astro-ph/0603018

Chen, C.-H. R., Indebetouw, R., Chu, Y.-H., et al. 2010, The Astrophysical Journal, 721, 1206, doi: 10.1088/0004-637x/721/2/1206

Cignoni, M., Sabbi, E., van der Marel, R. P., et al. 2015, ApJ, 811, 76, doi: 10.1088/0004-637X/811/2/76

de Grijs, R., Wicker, J. E., & Bono, G. 2014, The Astronomical Journal, 147, 122, doi: 10.1088/0004-6256/147/5/122

Dobashi, K., Shimoikura, T., Katakura, S., Nakamura, F., & Shimajiri, Y. 2019, PASJ, 71, S12, doi: 10.1093/pasj/psz041

Frerking, M. A., Langer, W. D., & Wilson, R. W. 1982, ApJ, 262, 590, doi: 10.1086/160451

Fujita, S., Torii, K., Kuno, N., et al. 2021, PASJ, 73, S172, doi: 10.1093/pasj/psz028

Fukui, Y., Habe, A., Inoue, T., Enokiya, R., & Tachihara, K. 2021, PASJ, 73, S1, doi: 10.1093/pasj/psaa103

Fukui, Y., Tsuge, K., Sano, H., et al. 2017, Publications of the Astronomical Society of Japan, 69, doi: 10.1093/pasj/psx032

Fukui, Y., Kawamura, A., Minamidani, T., et al. 2008, The Astrophysical Journal Supplement Series, 178, 56, doi: 10.1086/589833

Fukui, Y., Harada, R., Tokuda, K., et al. 2015, The Astrophysical Journal, 807, L4, doi: 10.1088/2041-8205/807/1/l4

Fukui, Y., Torii, K., Hattori, Y., et al. 2018, The Astrophysical Journal, 859, 166, doi: 10.3847/1538-4357/aac217

Fukui, Y., Tokuda, K., Saigo, K., et al. 2019, The Astrophysical Journal, 886, 14, doi: 10.3847/1538-4357/ab4900

Fukushima, H., & Yajima, H. 2021, MNRAS, 506, 5512, doi: 10.1093/mnras/stab2099

Galametz, M., Schruba, A., De Breuck, C., et al. 2020, A&A, 643, A63, doi: 10.1051/0004-6361/202038641

Galván-Madrid, R., Liu, H. B., Zhang, Z. Y., et al. 2013, ApJ, 779, 121, doi: 10.1088/0004-637X/779/2/121

Ginsburg, A., Bressert, E., Bally, J., & Battersby, C. 2012, ApJL, 758, L29, doi: 10.1088/2041-8205/758/2/L29

Gordon, K. D., Roman-Duval, J., Bot, C., et al. 2014, The Astrophysical Journal, 797, 85, doi: 10.1088/0004-637x/797/2/85

Gruendl, R. A., & Chu, Y.-H. 2009, ApJS, 184, 172, doi: 10.1088/0067-0049/184/1/172

Herrera, C. N., Rubio, M., Bolatto, A. D., et al. 2013, Astronomy & Astrophysics, 554, A91, doi: 10.1051/0004-6361/201219381

Hirota, T., Machida, M. N., Matsushita, Y., et al. 2017, Nature Astronomy, 1, 0146, doi: 10.1038/s41550-017-0146

Hodge, P. W. 1961, ApJ, 133, 413, doi: 10.1086/147044

Hughes, A., Wong, T., Ott, J., et al. 2010, MNRAS, 406, 2065, doi: 10.1111/j.1365-2966.2010.16829.x

Hunter, D. A., Elmegreen, B. G., Dupuy, T. J., & Mortonson, M. 2003, AJ, 126, 1836, doi: 10.1086/378056

Indebetouw, R., Johnson, K. E., & Conti, P. 2004, AJ, 128, 2206, doi: 10.1086/424614

Indebetouw, R., Wong, T., Chen, C. H. R., et al. 2020, ApJ, 888, 56, doi: 10.3847/1538-4357/ab5db7

Indebetouw, R., Brogan, C., Chen, C.-H. R., et al. 2013, The Astrophysical Journal, 774, 73, doi: 10.1088/0004-637x/774/1/73

Inoue, T., Hennebelle, P., Fukui, Y., et al. 2018, PASJ, 70, S53, doi: 10.1093/pasj/psx089

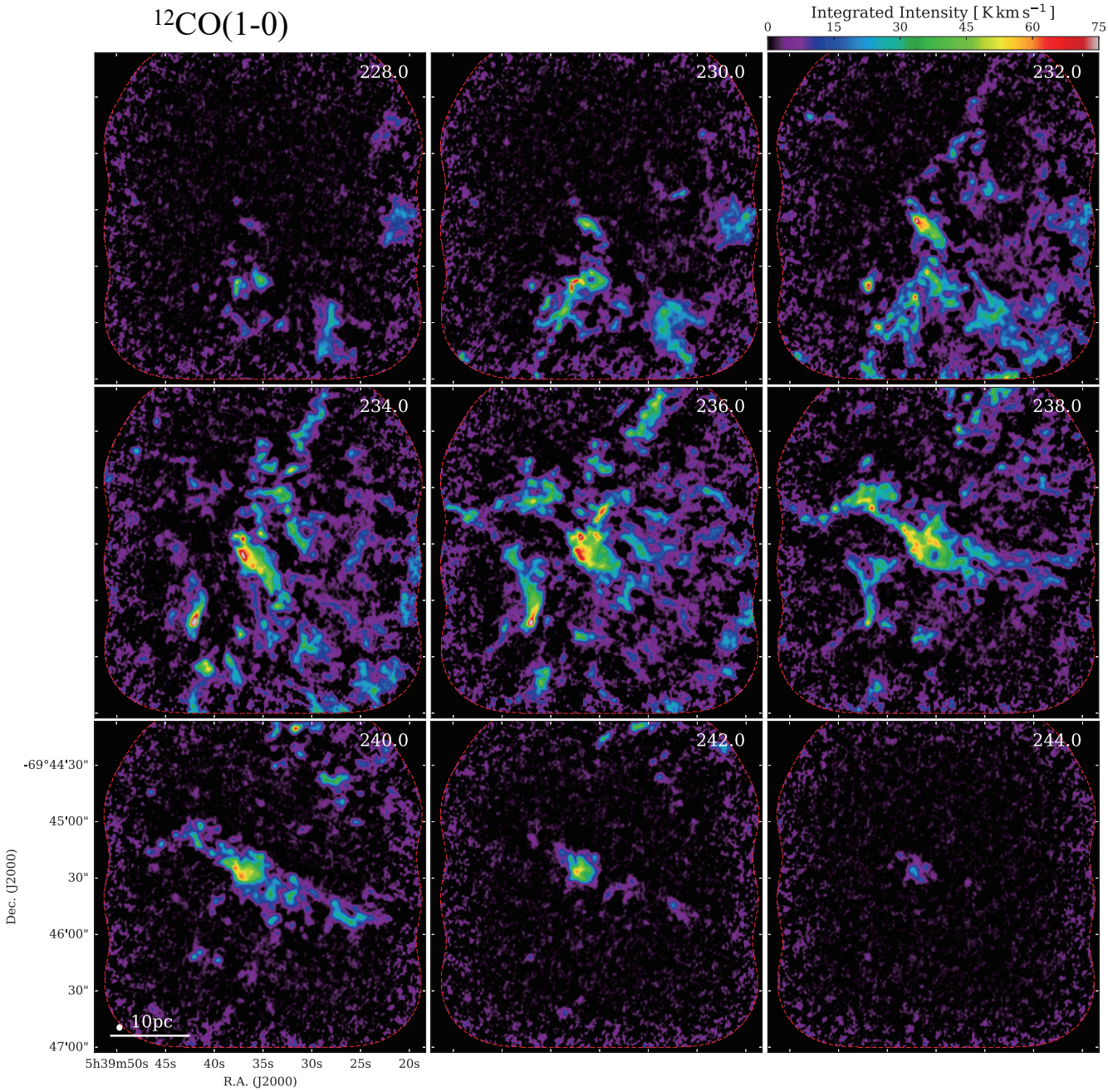

Figure 13. Velocity channel maps of N159W in ^{12}CO(J = 1–0). The lowest velocity in unit of km s^{-1} of each panel are given in the upper right corners. The white ellipse in the lower left corner in the lower left panel shows the beam size, 2.″2 × 1.″8, of the ^{12}CO data. Red dotted lines show the field coverage.

Johansson, L. E. B., Olofsson, H., Hjalmarson, A., Gredel, R., & Black, J. H. 1994, A&A, 291, 89

Johansson, L. E. B., Greve, A., Booth, R. S., et al. 1998, A&A, 331, 857

Jones, O. C., Woods, P. M., Kemper, F., et al. 2017, MNRAS, 470, 3250, doi: 10.1093/mnras/stx1101

Kawamura, A., Mizuno, Y., Minamidani, T., et al. 2009, The Astrophysical Journal Supplement Series, 184, 1, doi: 10.1088/0067-0049/184/1/1

Kohno, M., Tachihara, K., Torii, K., et al. 2021, PASJ, 73, S129, doi: 10.1093/pasj/psaa015

Kong, S., Arce, H. G., Maureira, M. J., et al. 2019, ApJ, 874, 104, doi: 10.3847/1538-4357/ab07b9

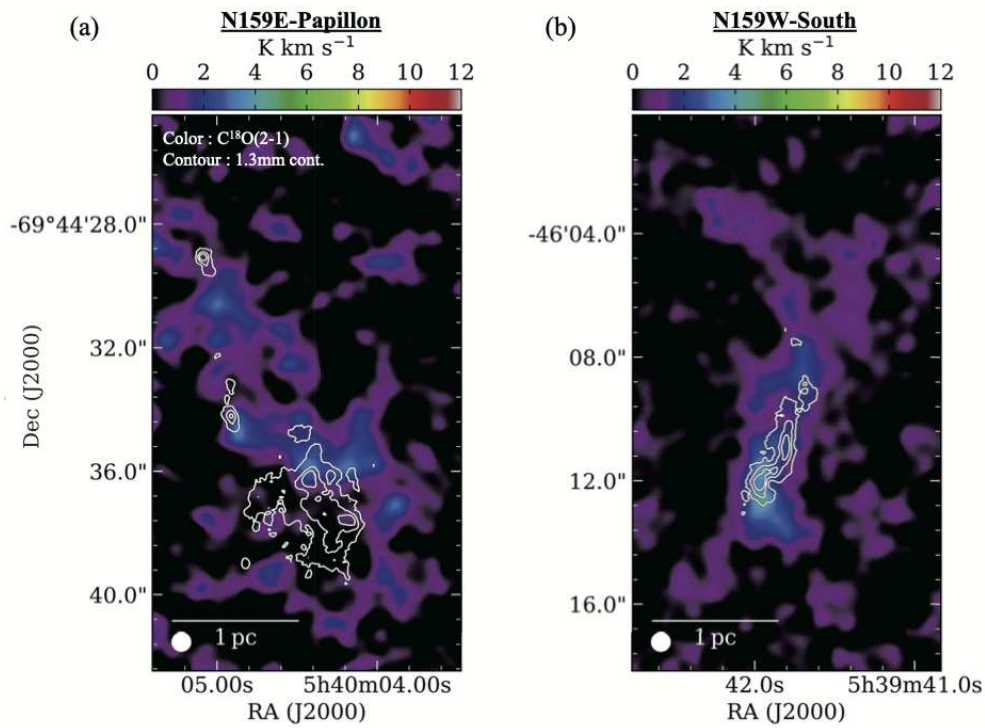

Figure 14. $C^{18}O$ and 1.3 mm continuum emission toward N159E-Papillon and N159W-South regions (Papers I; II). (a) The color-scale image shows the $C^{18}O$ velocity-integrated intensity map of N159E-Papillon with an angular resolution of 0.″6 shown in the lower left corner. The white contours show the 1.3 mm continuum emission. The lowest and subsequent contour steps are 0.15 mJy beam^{-1}. Note that we coordinate to the intensity scale with that in Figure 6a for the comparison purpose. (b) Same as panel (a), but for N159W-South.

Kong, S., Tan, J. C., Caselli, P., et al. 2017, ApJ, 834, 193, doi: 10.3847/1538-4357/834/2/193

Krumholz, M. R., & McKee, C. F. 2020, MNRAS, 494, 624, doi: 10.1093/mnras/staa659

Kumai, Y., Basu, B., & Fujimoto, M. 1993, ApJ, 404, 144, doi: 10.1086/172265

Lada, C. J., & Lada, E. A. 2003, ARA&A, 41, 57, doi: 10.1146/annurev.astro.41.011802.094844

Lee, E. J., Murray, N., & Rahman, M. 2012, The Astrophysical Journal, 752, 146, doi: 10.1088/0004-637x/752/2/146

Lee, M. Y., Madden, S. C., Lebouteiller, V., et al. 2016, A&A, 596, A85, doi: 10.1051/0004-6361/201628098

Longmore, S. N., Kruijssen, J. M. D., Bastian, N., et al. 2014, in Protostars and Planets VI, ed. H. Beuther, R. S. Klessen, C. P. Dullemond, & T. Henning, 291, doi: 10.2458/azu_uapress_9780816531240-ch013

Louvet, F., Motte, F., Hennebelle, P., et al. 2014, Astronomy & Astrophysics, 570, A15, doi: 10.1051/0004-6361/201423603

Maeda, R., Inoue, T., & Fukui, Y. 2021, ApJ, 908, 2, doi: 10.3847/1538-4357/abcc75

Matsushita, Y., Machida, M. N., Sakurai, Y., & Hosokawa, T. 2017, MNRAS, 470, 1026, doi: 10.1093/mnras/stx893

Matsushita, Y., Takahashi, S., Machida, M. N., & Tomisaka, K. 2019, ApJ, 871, 221, doi: 10.3847/1538-4357/aaf1b6

McKee, C. F., & Tan, J. C. 2003, ApJ, 585, 850, doi: 10.1086/346149

McMullin, J. P., Waters, B., Schiebel, D., Young, W., & Golap, K. 2007, in Astronomical Society of the Pacific Conference Series, Vol. 376, Astronomical Data Analysis Software and Systems XVI, ed. R. A. Shaw, F. Hill, & D. J. Bell, 127

Meixner, M., Gordon, K. D., Indebetouw, R., et al. 2006, AJ, 132, 2268, doi: 10.1086/508185

Millar, T. J., & Herbst, E. 1990, MNRAS, 242, 92, doi: 10.1093/mnras/242.2.92

Minamidani, T., Mizuno, N., Mizuno, Y., et al. 2008, The Astrophysical Journal Supplement Series, 175, 485, doi: 10.1086/524038

Minamidani, T., Tanaka, T., Mizuno, Y., et al. 2011, The Astronomical Journal, 141, 73, doi: 10.1088/0004-6256/141/3/73

Miyawaki, R., Hayashi, M., & Hasegawa, T. 2009, PASJ, 61, 39, doi: 10.1093/pasj/61.1.39

—. 2021, PASJ, doi: 10.1093/pasj/psab113

Mizuno, Y., Kawamura, A., Onishi, T., et al. 2010, PASJ, 62, 51, doi: 10.1093/pasj/62.1.51
Molet, J., Brouillet, N., Nony, T., et al. 2019, A&A, 626, A132, doi: 10.1051/0004-6361/201935497
Motogi, K., Hirota, T., Machida, M. N., et al. 2019, ApJL, 877, L25, doi: 10.3847/2041-8213/ab212f
Motte, F., Bontemps, S., & Louvet, F. 2018, Annual Review of Astronomy and Astrophysics, 56, 41, doi: 10.1146/annurev-astro-091916-055235
Motte, F., Schilke, P., & Lis, D. C. 2003, The Astrophysical Journal, 582, 277, doi: 10.1086/344538
Muraoka, K., Kondo, H., Tokuda, K., et al. 2020, The Astrophysical Journal, 903, 94, doi: 10.3847/1538-4357/abb822
Myers, P. C. 2009, The Astrophysical Journal, 700, 1609, doi: 10.1088/0004-637x/700/2/1609
Nayak, O., Meixner, M., Fukui, Y., et al. 2018, The Astrophysical Journal, 854, 154, doi: 10.3847/1538-4357/aaab5f
Nguyen-Luong, Q., Nguyen, H. V. V., Motte, F., et al. 2016, ApJ, 833, 23, doi: 10.3847/0004-637X/833/1/23
Nishimura, A., Tokuda, K., Kimura, K., et al. 2015, ApJS, 216, 18, doi: 10.1088/0067-0049/216/1/18
Nishimura, Y., Shimonishi, T., Watanabe, Y., et al. 2016, ApJ, 818, 161, doi: 10.3847/0004-637X/818/2/161
Ossenkopf, V., & Henning, T. 1994, A&A, 291, 943
Ott, J., Henkel, C., Staveley-Smith, L., & Weiß, A. 2010, ApJ, 710, 105, doi: 10.1088/0004-637X/710/1/105
Paron, S., Ortega, M. E., Fariña, C., et al. 2016, MNRAS, 455, 518, doi: 10.1093/mnras/stv2326
Peretto, N., Fuller, G. A., Duarte-Cabral, A., et al. 2013, Astronomy & Astrophysics, 555, A112, doi: 10.1051/0004-6361/201321318
Portegies Zwart, S. F., McMillan, S. L. W., & Gieles, M. 2010, ARA&A, 48, 431, doi: 10.1146/annurev-astro-081309-130834
Robitaille, T., & Bressert, E. 2012, APLpy: Astronomical Plotting Library in Python. http://ascl.net/1208.017
Rohlfs, K., & Wilson, T. L. 2004, Tools of radio astronomy
Saigo, K., Onishi, T., Nayak, O., et al. 2017, The Astrophysical Journal, 835, 108, doi: 10.3847/1538-4357/835/1/108
Schaefer, B. E. 2008, AJ, 135, 112, doi: 10.1088/0004-6256/135/1/112
Schneider, N., Csengeri, T., Bontemps, S., et al. 2010, Astronomy and Astrophysics, 520, A49, doi: 10.1051/0004-6361/201014481
Seale, J. P., Looney, L. W., Chu, Y.-H., et al. 2009, ApJ, 699, 150, doi: 10.1088/0004-637X/699/1/150
Seale, J. P., Meixner, M., Sewiło, M., et al. 2014, AJ, 148, 124, doi: 10.1088/0004-6256/148/6/124
Sewiło, M., Indebetouw, R., Charnley, S. B., et al. 2018, ApJL, 853, L19, doi: 10.3847/2041-8213/aaa079
Sharda, P., Menon, S. H., Federrath, C., et al. 2021, MNRAS, doi: 10.1093/mnras/stab3048
Smith, R. C., & MCELS Team. 1999, in New Views of the Magellanic Clouds, ed. Y. H. Chu, N. Suntzeff, J. Hesser, & D. Bohlender, Vol. 190, 28
Takahira, K., Tasker, E. J., & Habe, A. 2014, The Astrophysical Journal, 792, 63, doi: 10.1088/0004-637x/792/1/63
Tan, J. C., Beltrán, M. T., Caselli, P., et al. 2014, in Protostars and Planets VI (University of Arizona Press), doi: 10.2458/azu_uapress_9780816531240-ch007
Tanaka, K. E. I., Zhang, Y., Hirota, T., et al. 2020, ApJL, 900, L2, doi: 10.3847/2041-8213/abadfc
Tokuda, K., Onishi, T., Saigo, K., et al. 2018, The Astrophysical Journal, 862, 8, doi: 10.3847/1538-4357/aac898
Tokuda, K., Fukui, Y., Harada, R., et al. 2019, The Astrophysical Journal, 886, 15, doi: 10.3847/1538-4357/ab48ff
Tokuda, K., Muraoka, K., Kondo, H., et al. 2020, ApJ, 896, 36, doi: 10.3847/1538-4357/ab8ad3
Tokuda, K., Kondo, H., Ohno, T., et al. 2021, ApJ, 922, 171, doi: 10.3847/1538-4357/ac1ff4
Torii, K., Tokuda, K., Tachihara, K., Onishi, T., & Fukui, Y. 2021, PASJ, 73, 205, doi: 10.1093/pasj/psaa115
Torii, K., Hattori, Y., Hasegawa, K., et al. 2017, The Astrophysical Journal, 835, 142, doi: 10.3847/1538-4357/835/2/142
Tsuge, K., Sano, H., Tachihara, K., et al. 2019, The Astrophysical Journal, 871, 44, doi: 10.3847/1538-4357/aaf4fb
van den Bergh, S. 1981, A&AS, 46, 79
Vázquez-Semadeni, E., Palau, A., Ballesteros-Paredes, J., Gómez, G. C., & Zamora-Avilés, M. 2019, MNRAS, 490, 3061, doi: 10.1093/mnras/stz2736
Wong, T., Hughes, A., Ott, J., et al. 2011, The Astrophysical Journal Supplement Series, 197, 16, doi: 10.1088/0067-0049/197/2/16
Young, K. E., Lee, J.-E., Evans, Neal J., I., Goldsmith, P. F., & Doty, S. D. 2004, ApJ, 614, 252, doi: 10.1086/423609
Zhang, S., Zavagno, A., López-Sepulcre, A., et al. 2021, A&A, 646, A25, doi: 10.1051/0004-6361/202038421
Zinnecker, H., & Yorke, H. W. 2007, Annual Review of Astronomy and Astrophysics, 45, 481, doi: 10.1146/annurev.astro.44.051905.092549